[Si II], [Fe II], [C II], AND H₂ EMISSION FROM MASSIVE STAR-FORMING REGIONS

MICHAEL J. KAUFMAN,[1,2] MARK. G. WOLFIRE,[3] AND DAVID J. HOLLENBACH[2]

ABSTRACT

We calculate the [Si II] 34.8 μm, [Fe II] 26.0 μm, and [C II] 158 μm infrared fine-structure emission that may arise from ionized gas (H II regions) and/or associated neutral gas (photodissociation regions [PDRs]) in massive star-forming regions. Assuming thermal pressure balance between an H II region and a PDR, the relative amounts of fine-structure line emission from the H II region and PDR depend on the electron density and resulting thermal pressure in the H II region, gas-phase abundances of the emitting species, and the UV spectrum from the stellar population producing the H II region. For normal metallicity, we find that [C II] emission is always dominated by PDRs, while [Si II] and [Fe II] are dominated by PDRs for H II regions with electron density $n_e \gtrsim 10 \text{ cm}^{-3}$. We also calculate the H₂ 0–0 S(0), 0–0 S(1), 0–0 S(2), and 0–0 S(3) pure rotational line emission arising from the PDR at the atomic-to-molecular interface. The overall intensity of the H₂ line emission directly traces warm molecular mass, while H₂ line ratios constrain the PDR temperature, gas density, and far-ultraviolet field strength. Models of the integrated emission of [Si II], [Fe II], [C II], and H₂ from Galactic and extragalactic star-forming regions are presented for use in interpreting observations with *Spitzer*, *ISO*, SOFIA, and the *Herschel Space Observatory*. We compare our results with observations of the Galactic source NGC 2023 (an individual H II/photodissociation region in Orion), the inner regions of the Milky Way, and the central regions of the nearby star-forming spiral galaxy NGC 7331. We also compare our results with recently published similar work by Abel and coworkers.

Subject headings: galaxies: ISM — infrared: ISM — ISM: atoms — ISM: lines and bands — ISM: molecules

1. INTRODUCTION

Ultraviolet photons from young, hot stars play an important role in controlling the structure and emission spectra of the interstellar medium (ISM). The most obvious expressions of this influence are H II regions, the ionized gas surrounding massive star-forming regions. The sharp edges of H II regions mark the limit of influence of H-ionizing or EUV photons ($h\nu \geq 13.6$ eV), but far-ultraviolet (FUV) photons (6 eV $\leq h\nu < 13.6$ eV) play important roles in the chemistry, heating, and ionization balance of photodissociation regions (PDRs) that lie beyond the H II regions. PDRs include the neutral dense gas near sources of intense FUV illumination and the neutral diffuse ISM (e.g., Tielens & Hollenbach 1985; Parravano et al. 2003; Wolfire et al. 2003). Extensive modeling efforts have gone into understanding the physical processes controlling the emission from H II regions and PDRs, and mature tools are now available for computing the intensities of infrared emission lines from these regions (e.g., Sternberg 2004; Péquignot et al. 2001 and references therein; see also the results of the Leiden PDR Comparison Workshop, M. Röllig et al. 2006, in preparation).

In a paper on the ISM in starburst nuclei, Carral et al. (1994) presented an analysis of the relative contributions of H II regions and their surrounding PDRs to [C II] 158 μm emission and concluded that the neighboring PDRs dominated the emission for most conditions of interest. In this paper we compute the relative contributions of H II regions and their associated PDRs to the emission from [Si II] 35 μm, [Fe II] 26 μm, and [C II] 158 μm. We also compute the H₂ pure rotational emission from the PDRs. In § 2 we discuss the details of our PDR model, including recent

updates. We also discuss the Starburst99/Mappings models used for computing H II region emission, as well as the FUV field incident on the PDR, and our technique for merging the results of the two models. In § 3 we show results for a standard case, as well as for a range of model parameters, including electron densities, star cluster properties (i.e., UV spectrum), and metallicity. We also include a comparison between our results and those of Abel et al. (2005), who have undertaken similar calculations using a different H II region/PDR model. In § 4 we discuss the implications of our results for analysis of Galactic and extragalactic infrared observations, and we compare our predictions with results from the *Infrared Space Observatory* (*ISO*), *COBE*, and the *Spitzer Space Telescope* for the exemplary sources NGC 2023, the inner regions of the Milky Way, and NGC 7331.

2. MODELING THE H II REGION/PDR INTERFACE

2.1. *PDR Model*

For calculations of the emission from PDRs, we use an updated version of the PDR model originally developed by Tielens & Hollenbach (1985) and modified by Hollenbach et al. (1991), Burton et al. (1990), and Kaufman et al. (1999, hereafter K99). We have recently updated the code to provide a more accurate representation of H₂ level populations and emission. The model computes a simultaneous solution for the chemistry, radiative transfer, and thermal balance in PDRs. Assuming gas-phase elemental abundances and grain properties, each PDR model is essentially described by a constant density of H nuclei, n (or, alternatively, a constant thermal pressure, nT), and the incident FUV (6 eV $\leq h\nu < 13.6$ eV) flux, G_0, in units of 1.6×10^{-3} ergs cm^{-2} s^{-1}, which is approximately the local interstellar field (Habing 1968; Parravano et al. 2003).

These models have been used in the past to show how the structure of a molecular cloud varies with increasing optical depth from the cloud surface. Tielens & Hollenbach (1985) and Hollenbach et al. (1991) described the general morphology of

[1] Department of Physics, San Jose State University, One Washington Square, San Jose, CA 95192-0106.
[2] Space Science and Astrobiology Division, MS 245-3, NASA Ames Research Center, Moffett Field, CA 94035.
[3] Department of Astronomy, University of Maryland, College Park, MD 20742.

TABLE 1
Gas-Phase Abundances of Important Species

Species	Symbol	Value
Carbon[a]	x_C	1.4×10^{-4}
Oxygen[a]	x_O	3.2×10^{-4}
Silicon[a]	x_{Si}	1.7×10^{-6}
Iron[a]	x_{Fe}	1.7×10^{-7}
PAHs	$x_{PAH} = n_{PAH}/n$	6.0×10^{-7}

[a] Gas-phase abundances relative to H nuclei from Savage & Sembach (1996).

the surface layers for typical ratios $G_0/n \gtrsim 10^{-2}$ cm^3, as is often the case: an outer layer ($A_V \sim 1$) of atomic H, C$^+$, and O, a central layer where the H makes the transition to H$_2$ ($A_V \sim 1-2$) and where C$^+$ becomes a C/CO mixture ($A_V \sim 2-4$), and an inner layer ($A_V \sim 3-10$) where the carbon is mostly in CO and where any oxygen not incorporated into CO is primarily atomic due to photodissociation of other oxygen-bearing molecules by FUV photons. At larger depths, we leave the PDR and enter the very opaque molecular cores where the chemistry and heating are dominated by cosmic rays and where heavy gas-phase elements like O and C may freeze out on grain surfaces to form ices (e.g., Bergin et al. 2000; Jørgensen et al. 2004).

The PDR emission of interest in this paper is produced in the outer layers ($A_V \lesssim 1$), where carbon, silicon, and iron are singly ionized and the gas temperature is high ($T \gtrsim 100$ K), producing [C II] 158 μm, [Si II] 35 μm, and [Fe II] 26 μm emission. Near $A_V \sim 1$, the H I/H$_2$ transition occurs, and much of the H$_2$ pure rotational and rovibrational emission is produced; significant [C II] emission can also be produced here, although the gas is generally too cold to produce much extra [Si II] or [Fe II] emission. We note that the first ionization potentials for carbon, silicon, and iron are 11.26, 8.15, and 7.87 eV, respectively. Therefore, although hydrogen is neutral in PDRs, FUV photons can maintain most carbon, silicon, and iron as the ions C$^+$, Si$^+$, and Fe$^+$ in PDRs.

2.1.1. [Si II] 35 μm, [Fe II] 26 μm, and [C II] 158 μm Emission from PDRs

In an earlier paper (K99) we presented a detailed treatment of the emission from important PDR coolants from various layers within the PDR. Results were shown over a wide parameter space in G_0 and n, from conditions appropriate for the diffuse ISM up to those typical of massive-star–forming regions and starburst nuclei. Not included in that paper were the less intense fine-structure lines of [Si II] and [Fe II]. Although they are not dominant coolants anywhere in the parameter space, they are important diagnostics of the physical conditions in PDRs and are potentially detectable with the Infrared Spectrometer (IRS) on board the *Spitzer Space Telescope* and with spectrometers on future observatories. We present here the PDR intensities of the [Si II] 35 μm and [Fe II] 26 μm fine-structure transitions.

The gas-phase C, Si, and Fe abundances were taken from UV absorption measurements of diffuse and translucent clouds in the solar neighborhood (Savage & Sembach 1996) and are given in Table 1. We have taken polycyclic aromatic hydrocarbon (PAH) abundances from Wolfire et al. (2003); the PAHs affect the heating of the surface and the ionization structure through mutual neutralization and charge transfer reactions. In § 2.2 we compute the associated emission from H II regions for comparison, assuming the same gas-phase abundances in both H II regions and PDRs. Because [Si II] and [Fe II] are not dominant coolants and the
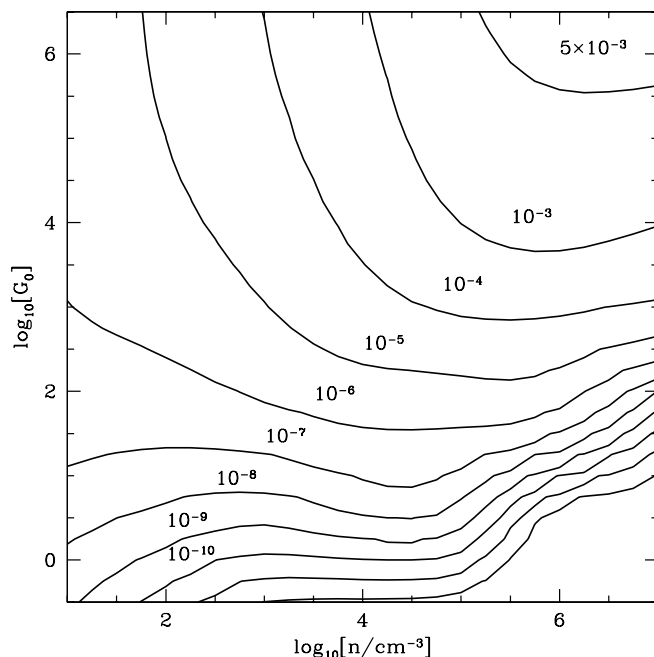

Fig. 1.—[Si II] 34.8 μm line intensity, in ergs s^{-1} cm^{-2} sr^{-1}, as a function of hydrogen nucleus density n and FUV radiation field G_0.

lines are optically thin, their line intensities scale as the adopted abundances.

A detailed description of the PDR model and the resulting temperature and abundance profiles appears in K99. For the following discussion of the [Si II] and [Fe II] emission, we refer the reader to Figures 2 and 3 and associated text of K99, where the behavior of [C II] emission was described as a function of G_0 and n. Both [Si II] and [Fe II] emissions behave similarly to [C II], with slight differences due to different excitations and critical densities. We note that for $n \lesssim 3 \times 10^3$ cm^{-3} and for FUV fields $G_0 \lesssim 300$, [C II] 158 μm is the dominant gas coolant, which as noted is never the case for [Si II] 34 μm and [Fe II] 26 μm. Since [C II] emission dominates the cooling in this regime, the gas temperature adjusts so that the emergent [C II] flux is just equal to the product of G_0 and the photoelectric heating efficiency (see Fig. 6 of K99). [Si II] and [Fe II], on the other hand, drop rapidly with decreasing G_0 (and therefore T), since their upper state energies are much higher than that of [C II], and also with decreasing density, since both are in the subthermal regime.

Figures 1 and 2 show the [Si II] and [Fe II] intensities as a function of G_0 and n, as determined from our constant density PDR models. (We have also run constant pressure models and find that the results do not vary significantly since both arise from surface layers where the temperature has not dropped substantially.) Both the [Si II] 35 μm and [Fe II] 26 μm emissions are optically thin, so the line intensities scale approximately as $I \propto N_i e^{-E_u/kT}/[1 + (n_{H,cr}/n_H)]$, where N_i is the column density of species i, E_u/k is the energy of the transition upper state in temperature units, n_H is the density of H atoms, and $n_{H,cr}$ is the critical density of the transition for H atom collisions. Both the [Si II] 35 μm and [Fe II] 26 μm lines are ground-state transitions, and thus the energy of the upper state, E_u/k, is equal to the energy of the transition $\Delta E/k$. For [Si II] 35 μm, $\Delta E/k \sim 410$ K and $n_{H,cr} \sim 3 \times 10^5$ cm^{-3}, while for [Fe II] 26 μm, $\Delta E/k \sim 550$ K and $n_{H,cr} \sim 2 \times 10^6$ cm^{-3} (see Table 2). In Figures 1 and 2, the dependence on column density, temperature, and density may be seen coming into play. For values of $G_0/n \gtrsim 10^{-3}$ cm^3, essentially

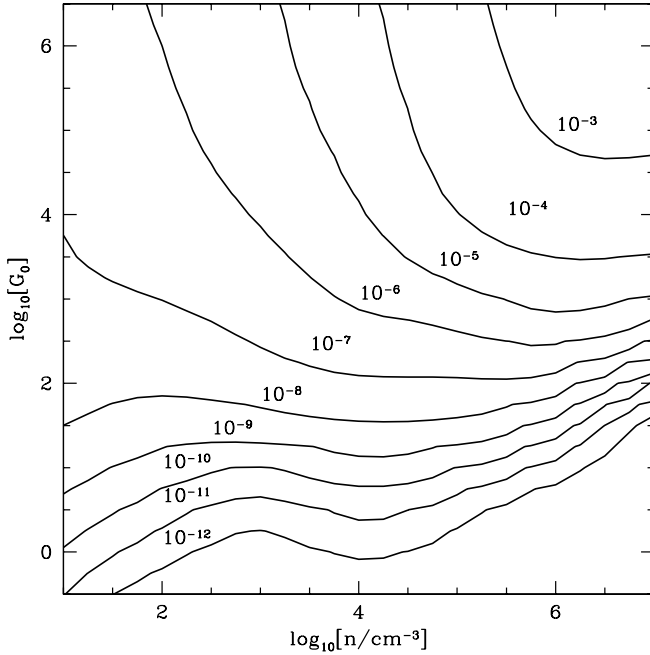Fig. 2.—[Fe II] 26.0 μm line intensity, in ergs s^{-1} cm^{-2} sr^{-1}, as a function of hydrogen nucleus density n and FUV radiation field G_0.

TABLE 2
Fine-Structure and Molecular Transitions

Species	Transition	$E_{\rm upper}$ (K)	λ (μm)	$n_{\rm H,cr}$[a] (cm^{-3})	$n_{e,\rm cr}$[b] (cm^{-3})
C$^+$	$^2P_{1/2}-^2P_{3/2}$	94	157.7	3.0E3	5.3E1
Si$^+$	$^2P_{1/2}-^2P_{3/2}$	410	34.8	2.6E5	1.2E3
Fe$^+$	$^6D_{9/2}-^6D_{7/2}$	550	26.0	2.2E6	1.2E4
H$_2$	0–0 $S(0)$	510	28.2	6.7E2	...
H$_2$	0–0 $S(1)$	1015	17.0	2.3E4	...
H$_2$	0–0 $S(2)$	1682	12.3	2.2E5	...
H$_2$	0–0 $S(3)$	2504	9.66	9.4E5	...

[a] Critical density for collisions with H atoms at 100 K for C$^+$, Si$^+$, and Fe$^+$ and at 300 K for H$_2$.
[b] Critical density for collisions with electrons at 10^4 K.

changes. For example, with $n = 10^3$ cm^{-3} and $G_0 = 1$, the surface temperature increases from $\sim$32 to $\sim$40 K when going from normal to high metallicity. This small change in temperature results in a factor of $\sim$10 increase in the [Si II] and [Fe II] intensities since the upper states of the transitions lie hundreds of degrees above ground. When the surface temperature lies well above the energy of the upper state, i.e., for FUV fields $G_0 \gtrsim 10^4$, there is little difference in the intensity between normal and high metallicity. For intermediate conditions, the high-metallicity cases have intensities $\sim$2–3 times higher than in the normal metallicity cases.

2.1.2. *Treatment of Molecular Hydrogen*

Detailed models of the dissociation, excitation, and line emission of molecular hydrogen in PDRs have been presented by several research groups. Black & van Dishoeck (1987) and Sternberg & Dalgarno (1989) concentrated on the UV-pumped fluorescent line emission from rovibrational transitions for a variety of UV fields and densities. Le Bourlot et al. (1993) included purely rotational transitions (which can be either UV pumped or collisionally excited) in the output list of diagnostic line intensities. Draine & Bertoldi (1996) presented a detailed analysis of the H$_2$ dissociation rate and H$_2$ line intensities as a function of varying UV field strengths and gas densities but with a simple parameterized temperature distribution. Burton et al. (1990, 1992) calculated H$_2$ line intensities from purely rotational transitions using a detailed collisional excitation calculation for the lowest lying rotational and vibrational levels but an approximate model for fluorescent line emission based largely on the results of Black & van Dishoeck (1987). There has also been recent progress in adding H$_2$ emission to the CLOUDY photoionization code (Shaw et al. 2005). Over the broad range of (G_0, n) parameter space considered in this paper, the rotational and vibrational lines are produced by both collisional excitation and fluorescent excitation (sometimes modified by collisions), and a more detailed approach is necessary than used by us in the past.

Here we use the PDR code made available by the Meudon Group[4] to calculate the H$_2$ excitation, line emission, dissociation, and heating/cooling processes produced by the H$_2$ molecule. For every call to our chemistry and heating subroutines we transfer our gas temperatures and abundances to the more detailed H$_2$ code and substitute the resulting H$_2$ rates into our subroutines. The Meudon code calculates the H$_2$ pumping and dissociation based on the rates in Abgrall et al. (1992). The conversion of ortho to para H$_2$ on grain surfaces is treated as in

all of the C, Si, and Fe is singly ionized at the surface. The ion columns are then set by the gas column density at which dust has effectively diminished the ionizing radiation field. Carbon typically remains ionized to columns $N_{\rm H} \sim 3 \times 10^{21}$ cm^{-2} ($A_V \sim 1$–2), while Si and Fe remain ionized to larger columns since they are ionized by softer photons. The net result, however, is that the columns of these species are essentially constant (within a factor of 2 or so) over much of this parameter space. So long as dust grains control the attenuation of the FUV radiation, Si and Fe remain ionized in to $A_V \sim 3$–6, and the resulting column densities are a few times 10^{16} and a few times 10^{15} cm^{-2}, respectively (although not all of the column may be warm enough to emit efficiently). With relatively constant column densities, the intensities depend on the gas density relative to the critical density for each species and the upper state energy for each transition relative to the gas temperature. For $n < n_{\rm H,cr}$ the intensities scale with $ne^{-\Delta E/kT}$. However, a complicated thermal balance calculation determines how T varies with n, G_0, and depth into the cloud. Only at low values of $G_0/n \lesssim 10^{-3}$ cm^3 (lower right corner of Figs. 1 and 2) are the columns of these species significantly altered: negatively charged PAHs effectively neutralize C$^+$, Si$^+$, and Fe$^+$, lowering the columns of these metal cations and their resulting line intensities. The neutralization rate and the ion columns are controlled by the ratio of G_0/n in this region.

In addition to our standard models, we have also calculated the [C II], [Si II], and [Fe II] intensities for cases where the gas-phase abundances of metals, dust, and PAHs are 3 times our standard values (hereafter referred to as $Z = 3$), conditions meant to approximate those in high-metallicity regions such as the Galactic center and the central regions of other similar galaxies. [C II] is relatively insensitive to changes in metallicity, particularly in cases where it dominates the gas cooling; in such cases, the temperature in the PDR surface layers adjusts so that the emergent [C II] flux is nearly equal to the FUV flux multiplied by the gas heating efficiency. The $Z = 3$ cases always result in somewhat higher temperatures, due to increased photoelectric heating, and the [Si II] and [Fe II] intensities can be quite sensitive to these

[4] See http://aristote.obspm.fr/MIS.

Le Bourlot (2000). Additional model details are given in Le Bourlot et al. (1993) and Le Petit et al. (2002, 2006).

There is a large uncertainty in the rates for H_2 collisions with H atoms, especially for vibrational transitions. Martin & Mandy (1995) and Mandy & Martin (1993) presented quasi-classical trajectory calculations including reactive and nonreactive channels, while Le Bourlot et al. (1999) and Flower & Roueff (1998) carried out quantum mechanical calculations for nonreactive collisions with an approximate treatment for reactive rates. At $T \sim 450$ K the Boltzmann-averaged $v = 1 \rightarrow 0$ de-excitation rate from the quasi-classical treatment is a factor of ~ 36 higher than the quantum mechanical rate (including the estimated reactive terms). The quasi-classical calculation predicts the reactive rates to be about 2 times the nonreactive rates, while the estimate in Le Bourlot et al. (1999) sets the reactive rates to be at maximum equal to the nonreactive rates and getting smaller as the transition energy decreases. In general, quantum calculations are considered to be more accurate; on the other hand, the quantum calculations do not include the reactive channels. A laboratory measurement at $T = 300$ K from Heidner & Kasper (1972) lies a factor of ~ 60 higher than the quantum calculation (including reactive rates). Based on observations of the vibrationally excited H_2 in the Orion Bar, Allers et al. (2005) and B. T. Draine & F. Bertoldi (2006, in preparation) have argued that the collisional de-excitation rates must be closer to the laboratory measurements than suggested by the quantum calculations (for additional discussion see Flower & Roueff 1998; Le Bourlot et al. 1999). The Meudon group has provided fits to both sets of collision rates that include well-behaved extrapolations to low temperatures. For these calculations we have adopted the fits to the Mandy & Martin (1993) rates with a minor adjustment at low temperature. We multiply all $\Delta v \neq 0$ rates by a smooth function that has a value of 1 at $T = 1500$ and 2 at $T = 300$. This results in a Boltzmann-averaged $v = 1 \rightarrow 0$ de-excitation rate that is slightly higher than the measured value but within the quoted uncertainty. We also note that the rates adopted by Burton et al. (1990) are a factor of ~ 2 higher than the measured value and are comparable to Mandy & Martin (1993) at $T = 1500$ K. A summary of the calculations and measurements is shown in Figure 3. We have investigated the effect of the new collision rates on the H_2 1–0 $S(1)$ line. At densities $n \lesssim 10^3$ cm^{-2}, the effect is minimal since here FUV pumping populates the upper state of the transition. Only for higher densities and high UV fields does the new rate affect the rovibrational lines. Here the population of the upper state is determined either by collisions or by collisionally modified FUV pumping. The biggest difference occurs in the upper right corner of our contour plots ($n = 10^5$ cm^{-3}, $G_0 = 10^5$), where the new collision rate results in a 1–0 $S(1)$ intensity ~ 3 times that produced using the Le Bourlot fit. At all other (n, G_0) combinations, the effect is small.

Several modifications to the Meudon code were required in order to properly merge our codes and maintain consistency in several of the H_2 rates. First, we modified the radiation transfer to be that of a normally incident radiation field as assumed in K99. Second, we use only a single grain size of $a \sim 0.1$ μm in radius and a single grain temperature, calculated as in Hollenbach et al. (1991), whereas the Meudon code includes 12 grain bins of varying temperature, size, and abundance. The grain temperature is important in determining, for example, the residence time of adsorbed H_2 on grain surfaces and thus the rate of ortho-to-para conversion on grains (Le Bourlot 2000). Grains that are too hot eject the molecule before conversion can occur. We assumed that all grains have the same temperature but varied the total grain surface area that is included in this rate until a good match
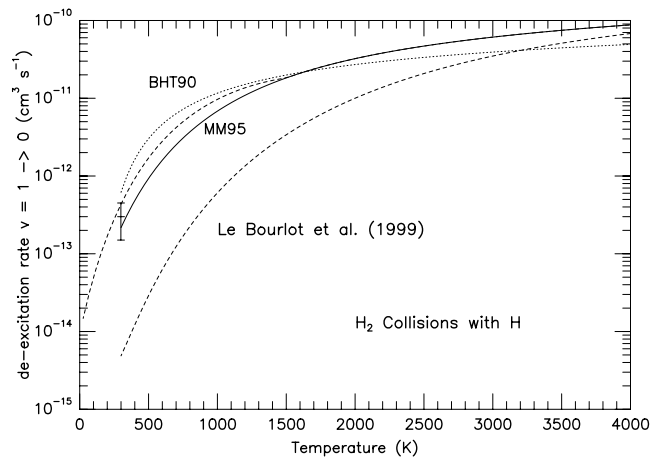

Fig. 3.—Comparison of Boltzmann-averaged collisional de-excitation rates. *Dotted line*: Rates from Burton et al. (1990). *Solid line*: Fit from Meudon code to the Martin & Mandy (1995) rates. *Lower dashed line*: Rate from Le Bourlot et al. (1999). *Upper dashed line*: Rate used in this paper, slightly modified from the Martin & Mandy (1995) fit. The point with error bars is the laboratory measurement of Heidner & Kasper (1972).

was achieved with our test case of NGC 2023 (as discussed below).

Two additional changes involve the H_2 formation rate on grains and the adsorption of H_2 molecules on grain surfaces. The Meudon code includes a detailed treatment of H_2 formation by first finding the abundance of atomic hydrogen adsorbed on grains (for each grain bin) and then calculating the interaction time to form an H_2 molecule. In the diffuse ISM the formation rate of molecular hydrogen on grains is $R = 3 \times 10^{-17}$ cm^3 s^{-1} (Jura 1975). Recent observations suggest that the H_2 formation rate in very dense PDRs like S140 may be somewhat higher, by a factor of 5, than that in the diffuse ISM (Habart et al. 2004). In light of these results, we have adopted a rate that is twice that in the diffuse ISM, i.e., $R = 6 \times 10^{-17} n_{H_1} n$ cm^3 s^{-1}, where n is the number density of H nuclei and n_{H_1} is the number density of atomic H. This H_2 formation rate is independent of temperature and is intended to include the offsetting effects of the H I collision rate with grains (which increases with temperature) and the efficiency with which H atoms stick to grains (which decreases with temperature). This rate is integrated over the grain distribution, and we ensured that the abundance of H I adsorbed on grains is consistent with this rate. We held this rate constant over our extended parameter space. We have also tested our line ratios with formation rates 5 times the rate in the diffuse ISM and found only minor changes between 2 and 5 times the diffuse ISM H_2 formation rate.

The Meudon code calculates the self-consistent abundance of H_2 on grains, for each grain bin, by balancing the adsorption rate with various desorption processes. We have adopted the adsorption rate of H_2 on grains from Burton et al. (1992): $R = 8.5 \times 10^{-17}(T/300 \text{ K})^{1/2} n_{H_2} n$ cm^{-3} s^{-1}, where the rate has been integrated over the grain size distribution. We have set the total H_2 abundance on grains to be consistent with our adsorption rate.

As one test of our code, we compared our calculated line intensities with the most recent online version of the Meudon code for the case of constant gas temperature $T = 50$ K, FUV field $G_0 = 10$, and gas density $n = 1.0 \times 10^3$ cm^{-3}. Due to the relatively low (constant) temperature, this procedure tests mainly the H_2 formation/dissociation and FUV pumping schemes. Assuming an isotropic radiation field (as assumed in the online Meudon case), we find that agreement is within 25% up to 0–0 $S(15)$. In
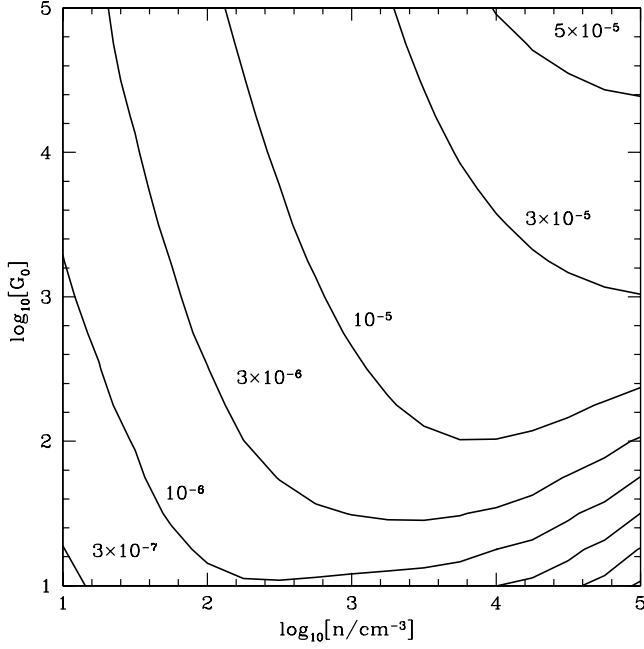
FIG. 4.—H$_2$ 0–0 $S(0)$ line intensity, in ergs s^{-1} cm^{-2} sr^{-1}, as a function of hydrogen nucleus density n and FUV radiation field G_0.
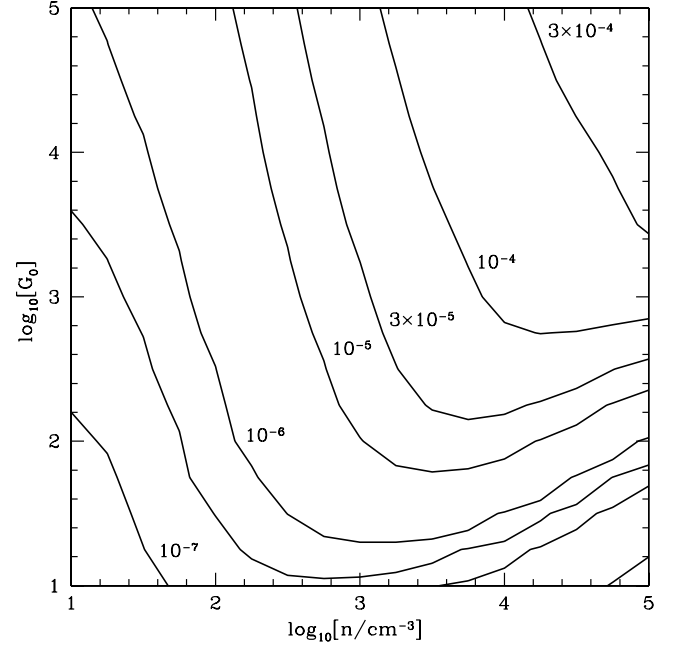

FIG. 5.—H$_2$ 0–0 $S(1)$ line intensity, in ergs s^{-1} cm^{-2} sr^{-1}, as a function of hydrogen nucleus density n and FUV radiation field G_0.

this paper, however, we assume a normally incident radiation field, which changes the line fluxes by factors <2.

As an additional test of our code, we compared our calculated H$_2$ column densities in the ground vibrational level with the observational and theoretical results presented by Draine & Bertoldi (2000) for the NGC 2023 PDR. We find that we can match the observational results to better than 40% for levels up to $j = 15$, using the same gas density as Draine & Bertoldi (2000) but an FUV field higher than theirs by a factor of 2. A detailed comparison between our results and those of Draine & Bertoldi (2000) is presented in § 4.1.

Figures 4, 5, 6, and 7 show the calculated line intensities for the H$_2$ 0–0 $S(0)$, 0–0 $S(1)$, 0–0 $S(2)$, and 0–0 $S(3)$ transitions as a function of the incident FUV field G_0 and gas density n. The general behavior of the contours can be understood from the discussion given in Burton et al. (1990); see in particular equations (23)–(29) of that paper, where the dependence of the line intensity is given in various n, T, and G_0 regimes. Transition zones occur at densities n greater than the critical density $n_{\rm H,cr}$ (for collisions with H I), at small ratios of G_0/n where H$_2$ self-shielding becomes important, and at gas temperatures greater than ~100 K where thermal excitation of the lines can contribute. The 0–0 $S(0)$ and 0–0 $S(1)$ line intensities result from collisionally modified FUV pumping (at low T or G_0) or from pure thermal excitation (at high T or G_0) since their upper states are relatively low lying and their critical densities are $\lesssim10^3$ cm^{-3} even at low temperatures. The 0–0 $S(2)$ and 0–0 $S(3)$ transitions arising from higher lying states are generally produced by FUV pumping since the critical densities and upper state energies are considerably larger. For $G_0/n \lesssim 10^{-2}$ cm^3, self-shielding of H$_2$ is important and the transition from H to H$_2$ occurs at columns $<10^{21}$ cm^{-2}, without the aid of dust opacity. Here the intensities of the FUV-pumped lines are proportional to G_0 since H$_2$ absorbs most of the pump photons. For $G_0/n \gtrsim 10^{-2}$ cm^3, dust absorbs most of the FUV photons capable of pumping H$_2$ transitions; H$_2$ has a low abundance to columns $N \sim 10^{21}$ cm^{-2} and can only absorb a small fraction of the pump photons. Here the intensities of the high-J H$_2$ lines scale with density and are independent of G_0. In equilibrium,

the column-integrated H$_2$ formation rate on grains [$\propto N({\rm H})n \propto n$] is proportional to the H$_2$ photodissociation rate, which is itself proportional to the pump rate per cm^2; since the intensities scale with the pump rate, they are thus proportional to n. Plots of the diagnostic line ratios 0–0 $S(1)$/0–0 $S(0)$, 0–0 $S(2)$/0–0 $S(0)$, and 0–0 $S(3)$/0–0 $S(1)$ are shown in Figures 8, 9, and 10, respectively.

We also show the line intensity for the 1–0 $S(1)$ rovibrational transition (Fig. 11). Over most of our parameter space the excitation of this emission line is dominated by FUV pumping to excited electronic states followed by fluorescence to vibrationally excited levels. We have not plotted the ratio 2–1 $S(1)$/1–0 $S(1)$ since it has a value of $\simeq0.5$ over most of our parameter
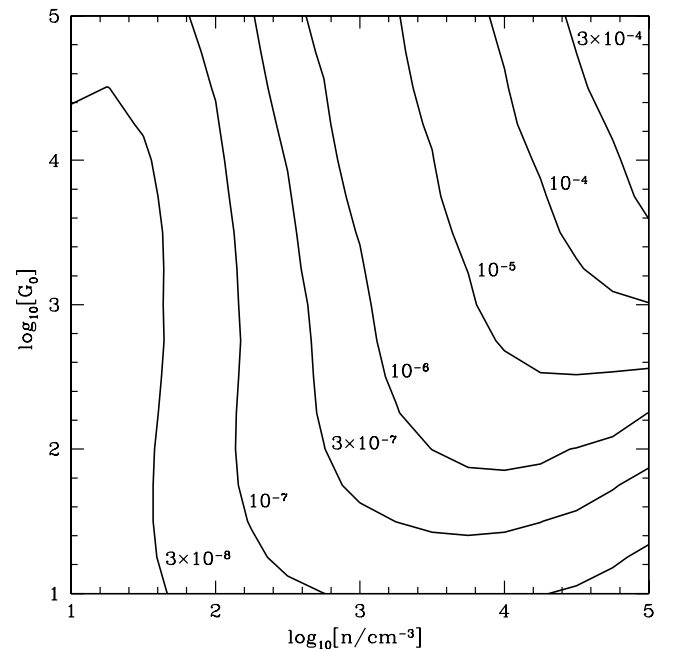

FIG. 6.—H$_2$ 0–0 $S(2)$ line intensity, in ergs s^{-1} cm^{-2} sr^{-1}, as a function of hydrogen nucleus density n and FUV radiation field G_0.
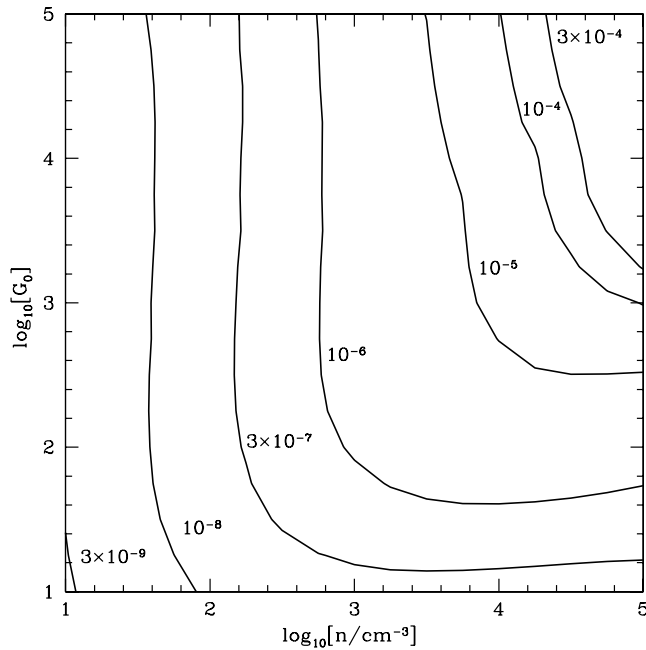
Fig. 7.—H_2 0–0 $S(3)$ line intensity, in ergs s^{-1} cm^{-2} sr^{-1}, as a function of hydrogen nucleus density n and FUV radiation field G_0.

Fig. 9.—H_2 0–0 $S(2)$/0–0 $S(0)$ line intensity ratio as a function of hydrogen nucleus density n and FUV radiation field G_0.

space.[5] This value is characteristic of FUV pumping where the emission depends on the radiative cascade through the transitions. However, at high density ($n \gtrsim 10^4$ cm^{-3}) and high FUV fields ($G_0 \gtrsim 10^4$) the gas temperatures are sufficiently high ($T \gtrsim 1000$ K) and collisions sufficiently frequent that the levels are thermally populated and the ratio drops to lower values. An intermediate case may occur at high density ($n \gtrsim 10^4$ cm^{-3}) but lower FUV fields where the temperature is not high enough for collisions to significantly populate excited states but where the

---

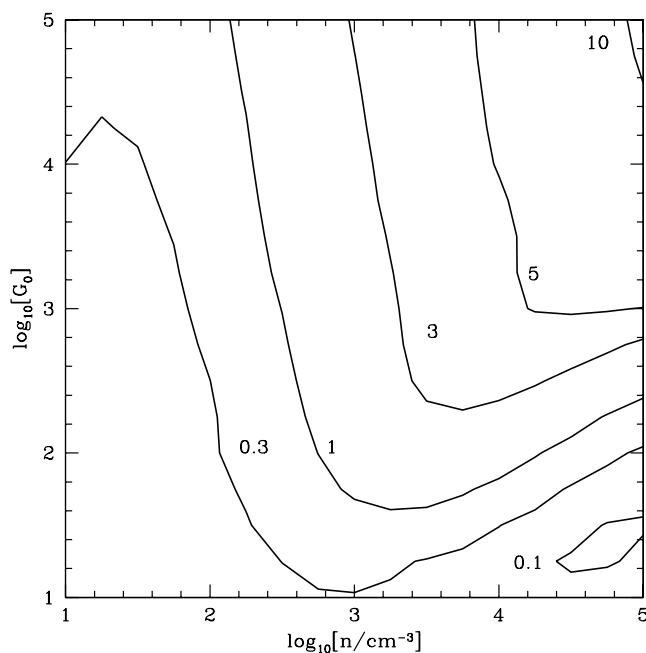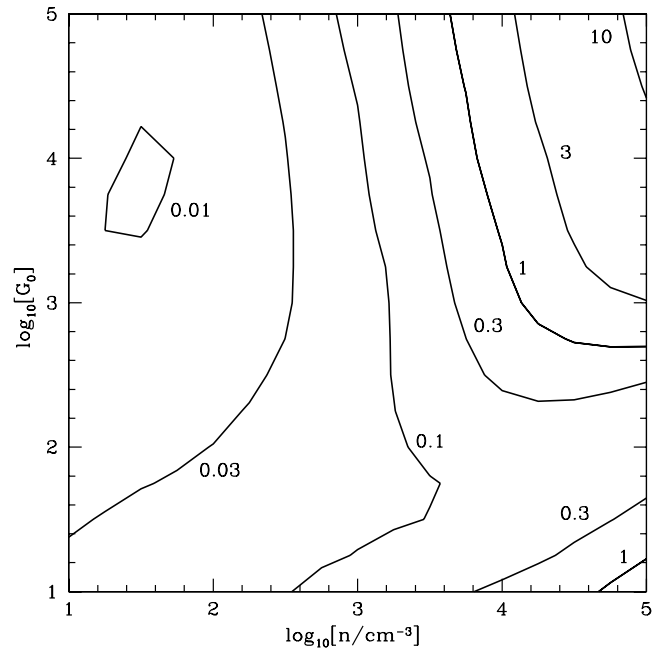[5] This ratio and many others of interest are available from the PDR Toolbox located at http://dustem.astro.umd.edu.

fluorescent spectrum is modified by collisional de-excitation (see discussion in Sternberg & Dalgarno 1989).

We have also computed the emission from H_2 for cases where the metallicity is 3 times our standard value ($Z = 3$). The intensities of the $S(0)$ and $S(1)$ lines, as well as the ratios $S(2)/S(0)$ and $S(3)/S(1)$, are shown in Figures 12, 13, 14, and 15, respectively. The principal differences between these figures and the standard cases arise from the increased H_2 formation rate due to the higher grain abundance. The result is larger line intensities for a given density since more H_2 forms in warmer surface gas. We discuss the implications of these results further in §§ 4.2 and 4.3.
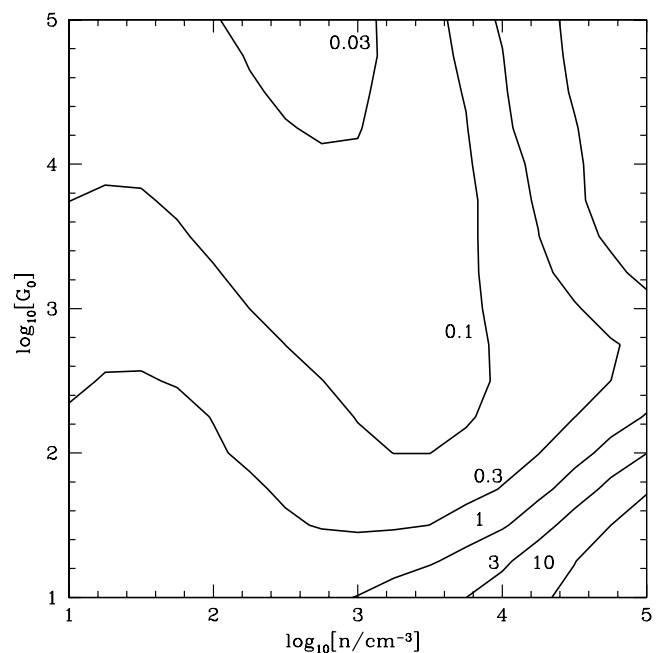

Fig. 8.—H_2 0–0 $S(1)$/0–0 $S(0)$ line intensity ratio as a function of hydrogen nucleus density n and FUV radiation field G_0.
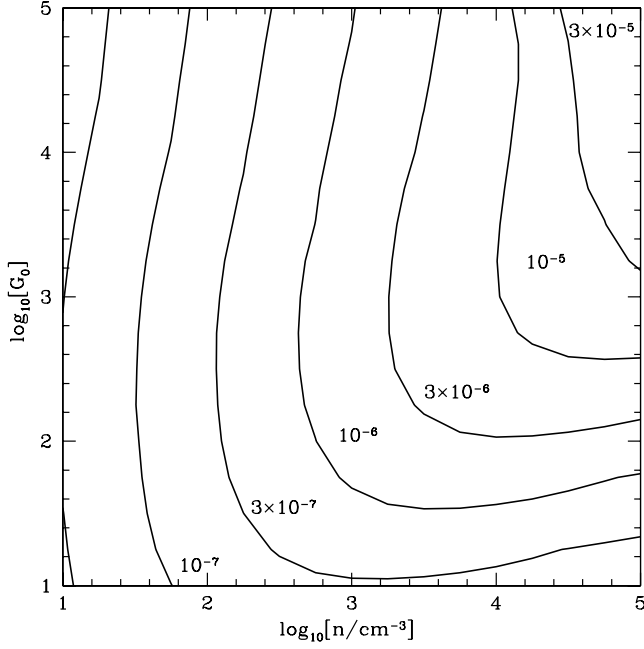

Fig. 10.—H_2 0–0 $S(3)$/0–0 $S(1)$ line intensity ratio as a function of hydrogen nucleus density n and FUV radiation field G_0.

FIG. 11.—H₂ 1–0 $S(1)$ line intensity, in ergs s^{-1} cm^{-2} sr^{-1}, as a function of hydrogen nucleus density n and FUV radiation field G_0.

FIG. 13.—H₂ 0–0 $S(1)$ line intensity as a function of hydrogen nucleus density n and FUV radiation field G_0, for models with metal abundances increased by a factor of 3.

2.2. H II Region Model

To compute the H II region emission, we used the Starburst99/ Mappings (Leitherer et al. 1999; L. Kewley et al. 2006, in preparation) models available from the Space Telescope Science Institute and the Institute for Astronomy.[6] Starburst99 allows the user to compute the composite spectrum of a star cluster; the spectrum is passed to the Mappings photoionization model, from which the nebular structure and resultant H II region emission spectrum are
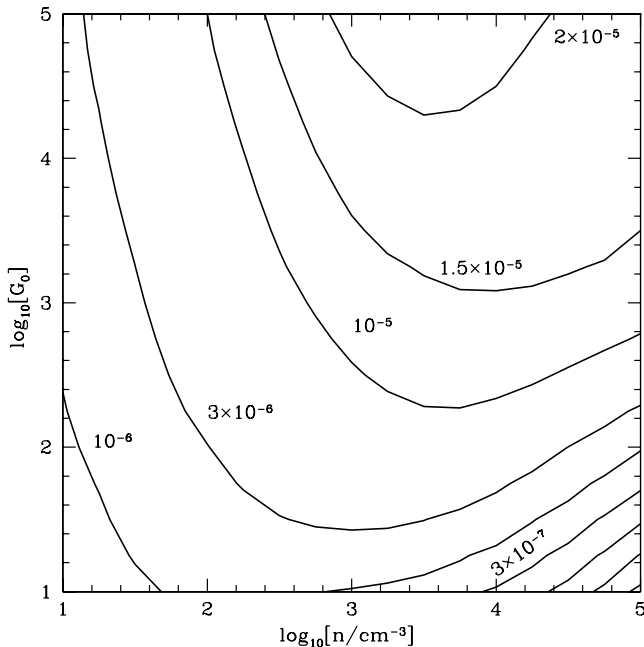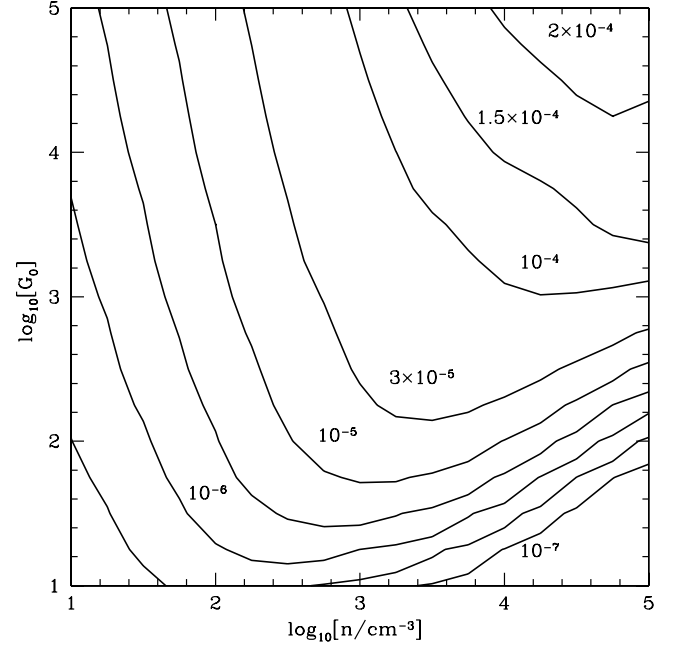
computed. The modeling tools allow the user to vary a number of inputs, including the properties of the star cluster responsible for the H II region and the properties of the ionized gas. The properties of the star cluster determine the ultraviolet spectrum produced by the cluster. In Starburst99, this is done by setting the initial mass function (IMF), the mass-loss rates, and the age of the cluster (to determine spectral shape) and then the size of the cluster to set the absolute luminosity Φ_i of ionizing EUV photons. The properties of the ionized gas that are input include the electron density, grains properties, and gas-phase abundances. The model outputs include the ionization and temperature structure, the Strömgren radius, and

[6] See http://www.stsci.edu/science/starburst99/mappings.

FIG. 12.—H₂ 0–0 $S(0)$ line intensity, in ergs s^{-1} cm^{-2} sr^{-1}, as a function of hydrogen nucleus density n and FUV radiation field G_0, for models with metal abundances increased by a factor of 3.
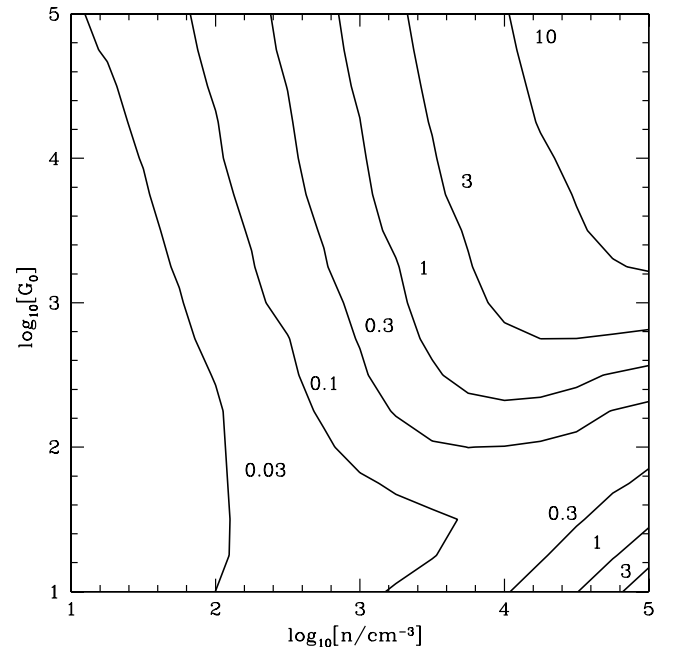

FIG. 14.—H₂ 0–0 $S(2)/0$–0 $S(0)$ line intensity ratio as a function of hydrogen nucleus density n and FUV radiation field G_0, for models with metal abundances increased by a factor of 3.

FIG. 15.—H_2 0–0 $S(3)$/0–0 $S(1)$ line intensity ratio as a function of hydrogen nucleus density n and FUV radiation field G_0, for models with metal abundances increased by a factor of 3.
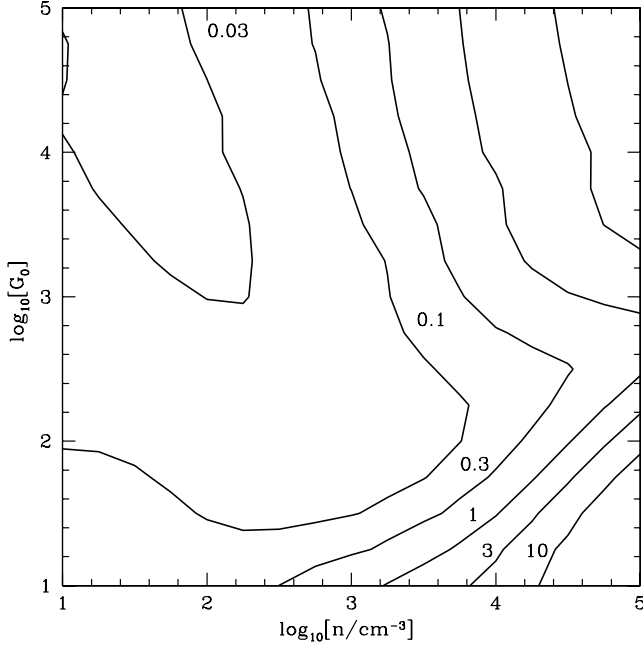

FIG. 16.—Schematic representation of the merged H II region and PDR models. $P_{\mathrm{H\,II}} = P_{\mathrm{PDR}}$. Starburst99 is used for the cluster spectrum. Mappings is used for the H II region structure; emitted H II region spectrum; [Fe II]$_{\mathrm{H\,II}}$, [Si II]$_{\mathrm{H\,II}}$, and [C II]$_{\mathrm{H\,II}}$ emission; and R_{S}. The emitted spectrum plus R_{S} gives G_0. Our PDR models give [Fe II]$_{\mathrm{PDR}}$, [Si II]$_{\mathrm{PDR}}$, [C II]$_{\mathrm{PDR}}$, and H_2 emission. A_V in the H II region is $\lesssim 1$, A_V in the PDR is $\gtrsim 2$, and A_V at the H I/H_2 boundary is $\lesssim 1$.

the strengths of emission lines from the H II region. The strengths of several hundred emission lines are computed, including those of the [C II] 158 μm, [Si II] 35 μm, and [Fe II] 26 μm fine-structure lines.

The principal input parameters to the models were Φ_i, which we varied between 10^{49} (roughly corresponding to small Trapezium-like clusters) and 10^{51} s^{-1} (corresponding to large clusters with ~ 100 O-type stars), and the electron density in the H II region, n_e, which we varied from 1 to 10^3 cm^{-3}. Our standard case has stars in the zero-age cluster up to $M_{\mathrm{max}} = 100\ M_\odot$, but our computations are made for a cluster age of 5 Myr, so that stars with mass $\gtrsim 30\ M_\odot$ have evolved off the main sequence. The resulting EUV spectrum is still relatively hard compared to a cluster with $M_{\mathrm{max}} \sim 25\ M_\odot$. (In § 3.2 we compare results for different values of M_{max}, as well as for our standard cluster at an earlier age and for regions with different metallicities.) The spectrum in each case is passed to Mappings, which calculates the H II region structure and emission lines resulting from the Starburst99 spectrum illuminating gas with our chosen electron density, gas-phase abundances, and grain properties. The gas-phase abundances chosen for the H II region match those in our standard PDR models (Table 1). We also present models for which the PDR and H II region metallicities and the dust and PAH abundances have been increased by a factor of 3 ($Z = 3$).

In H II regions, fine-structure lines are pumped by collisions with electrons. Temperatures in H II regions are $\sim 10^4$ K, much larger than $\Delta E/k$ for the transitions considered here, so the intensities are proportional to $N_i/(1 + n_{e,\mathrm{cr}}/n_e)$, where $n_{e,\mathrm{cr}}$ is the critical density for electron collisions and N_i is the column density of the species in the H II region. Values of $n_{e,\mathrm{cr}}$ are given in Table 2.

2.3. Merging the Models

Given the star cluster and H II region parameters, Starburst99/Mappings calculates the ionization structure of the nebula, from which we determine the Strömgren radius R_{S} (here defined as the point where H is 50% neutral, although the edge is very sharp). From the FUV spectrum of the star cluster, the column density of
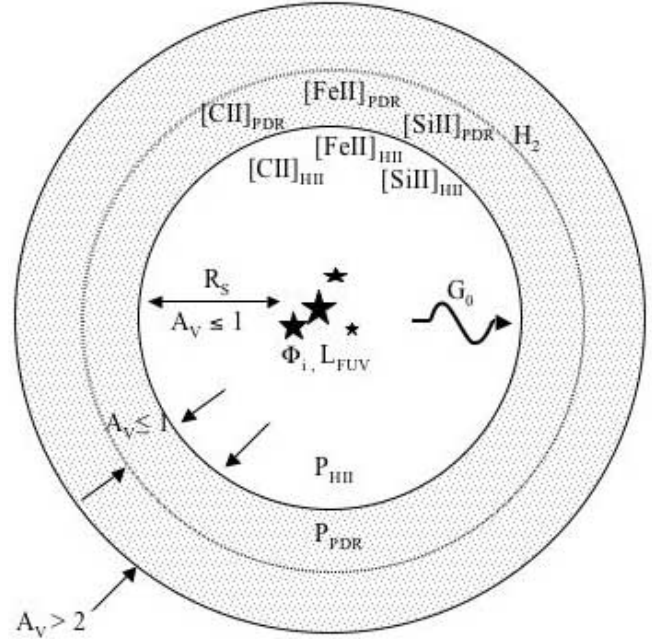
the H II region to R_{S}, and assuming standard dust extinction in the FUV, we compute the FUV flux, G_0, incident on the adjoining PDR surface (see Fig. 16). We equate the thermal pressure in the H II region, $2n_e T$, with the thermal pressure in the PDR gas, $n_{\mathrm{H}} T$ (see § 3.1 for a discussion of the transition from the H II region to the PDR). Thermal pressures run from $\sim 1.5 \times 10^4$ to $\sim 2 \times 10^7$ cm^{-3} K and are mostly sensitive to n_e since the H II region temperatures ($\sim 10^4$ K) are nearly constant (although in high-metallicity cases, $T_{\mathrm{H\,II}}$ is as much as 2 times lower, and the pressures are correspondingly lower). We have a precomputed grid of PDR models (K99) for which the thermal pressure at the surface is known as a function of n_{H} and G_0, so the pressure and FUV field given by the H II region model correspond to a unique PDR surface gas density. From our model of the PDR emission for that G_0 and n_{H}, we know the line flux emerging from the PDR surface in each of the diagnostic lines. We multiply the emergent PDR line fluxes by $4\pi R_{\mathrm{S}}^2$ (under the assumption that the PDR bounds the H II region on all sides and is sufficiently thick to absorb all of the FUV flux[7]) to calculate the PDR [C II], [Si II], and [Fe II] luminosities for comparison with those from the H II region. Note that the PDR is geometrically thin compared with the H II region so that the PDR is treated as a thin shell for the purpose of computing the PDR line emission.

3. RESULTS

3.1. Standard Case

To demonstrate the details of the merged model calculations, we first look in some detail at the results from a single model.

---

[7] We assume that the PDR extends to a visual extinction $A_V = 10$ so that the gas is completely molecular and dominated by cold cloud chemistry on the edge farther from the H II region. The exact choice of total A_V has little effect on the luminosities as long as it extends to $A_V \gtrsim 2$ since the lines presented here are produced primarily at $A_V \simeq 0$–2.
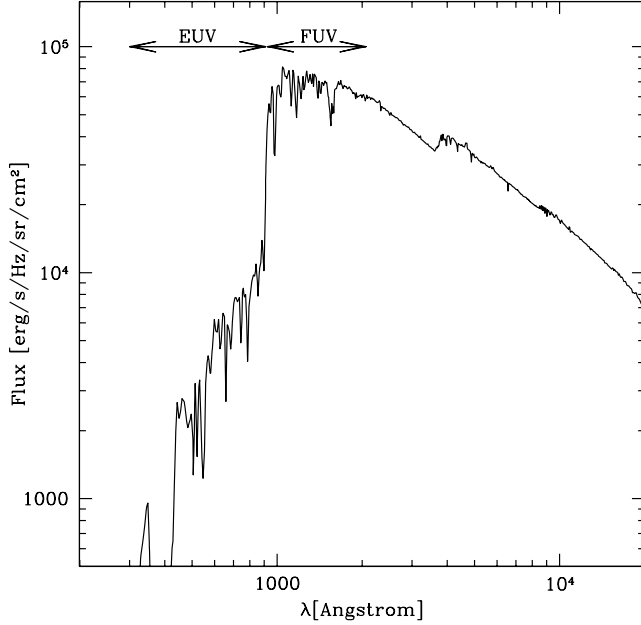
FIG. 17.—Spectrum of a star cluster producing $\Phi_i = 10^{49}$ H-ionizing (EUV) photons s^{-1}. This cluster produces $\sim 5 \times 10^5$ $L_\odot$ of FUV flux.

FIG. 18.—Structure of a merged H II region / PDR model, for H II region electron density $n_e = 10$ cm^{-3} and number of H-ionizing photons $\Phi_i = 10^{49}$ s^{-1}. The star cluster is to the left, and the H II region extends to $\sim 3.3 \times 10^{19}$ cm. The transition region (see § 3.1) is indicated by the dotted lines. *Top*: Temperature and density. *Middle*: Fraction of H nuclei that are ionized (H II), neutral atomic (H I), or molecular (H$_2$). *Bottom*: Fractional abundances of C$^+$, Si$^+$, and Fe$^+$.

Here we choose $\Phi_i = 10^{49}$ s^{-1} shining on a nebula with $n_e = 10$ cm^{-3}. We begin by running a Starburst99 model with standard star cluster conditions: $M_{\rm cluster} = 10^6$ $M_\odot$, $M_{\rm max} = 100$ $M_\odot$, and Salpeter IMF (power-law index of -2.35). The resulting spectrum is then integrated from 912 Å downward to find the number of ionizing photons, in this case $\sim 3.4 \times 10^{49}$ s^{-1}. Starburst99 is then rerun using the option that allows the number of stars in the star cluster to be scaled so as to adjust the ionizing luminosity. The stellar spectrum from 200 Å to 2 μm is shown in Figure 17. H I opacity in the stellar photospheres results in a steep decrease in stellar flux for $\lambda < 912$ Å, and most of the flux emerges in the FUV, from 912 to 2000 Å. The 5 Myr old cluster model (with $M_{\rm max} = 100$ $M_\odot$) gives $L_{\rm FUV} = 5.3 \times 10^5 \Phi_{49}$ $L_\odot$, where $\Phi_i = 10^{49} \Phi_{49}$ photons s^{-1}. Optical line emission from the H II region is dominated by H I and He I recombination lines, with smaller contributions from [O III], [O II], [Ne III], and [S III] forbidden lines. C, Si, and Fe remain doubly ionized throughout most of the H II region, with C$^+$, Si$^+$, and Fe$^+$ becoming the dominant ions of these species only near R_S (see Fig. 18), where the ionization parameter is low. [C II], [Si II], and [Fe II] excitation is dominated here by collisions with electrons.

In the H II region, the thermal pressure $P_{\rm H II} \simeq 2 n_e T_e = 1.6 \times 10^5$ cm^{-3} K. The FUV produced by the star cluster passes through the H II region and is extincted by a factor $e^{-1.8 A_V}$, where A_V is the visual extinction due to dust through the nebula; in this particular case, the FUV is about 25% weaker than it would be in the absence of dust. At R_S, and taking the extinction into account, the FUV flux at the interface is ~ 0.12 ergs s^{-1} cm^{-2} or $G_0 = 74$. Our precomputed models show that for this value of G_0, a surface pressure of 1.6×10^5 cm^{-3} K arises if the FUV shines on gas with H nuclei density of 1120 cm^{-3}. This model then predicts the [C II], [Si II], and [Fe II] intensities. In the PDR, these fine-structure lines are produced primarily through collisions with H atoms. As can be seen in Figure 18, the zone in which C$^+$, Si$^+$, and Fe$^+$ are abundant is quite narrow and the gas temperature drops below $\Delta E / k$ only a short distance into the PDR. As hydrogen in the PDR goes from H I to H$_2$, molecular hydrogen emission is also produced. Figure 19 shows the contributions to
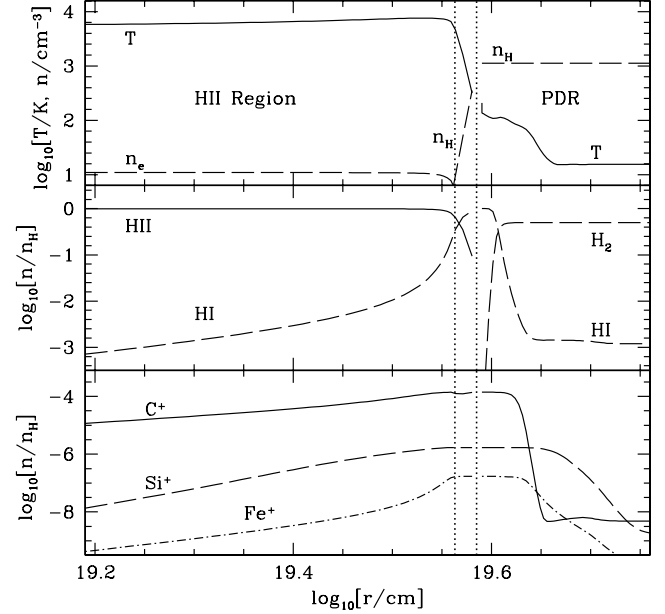
the luminosities of the fine-structure lines from the H II region and the PDR, as well as the H$_2$ emission from the PDR.

As may be seen in Figure 18, there exists a transition region between the H II region and the PDR, where the electron abundance drops to $\lesssim 0.5$ but before we begin computing the PDR structure (where $x_e \sim x_{\rm C} \sim 1.4 \times 10^{-4}$). In this transition zone, the temperature drops from $\sim 10^4$ to $\lesssim 1000$ K and x_e drops from 0.5 to $\sim 10^{-4}$. The Mappings code only computes the fine-structure emission due to electron collisions in the hot gas, but there is also the possibility that collisions with H atoms in the transition zone may contribute significant line emission. To maintain consistency with our assumption of pressure equilibrium between
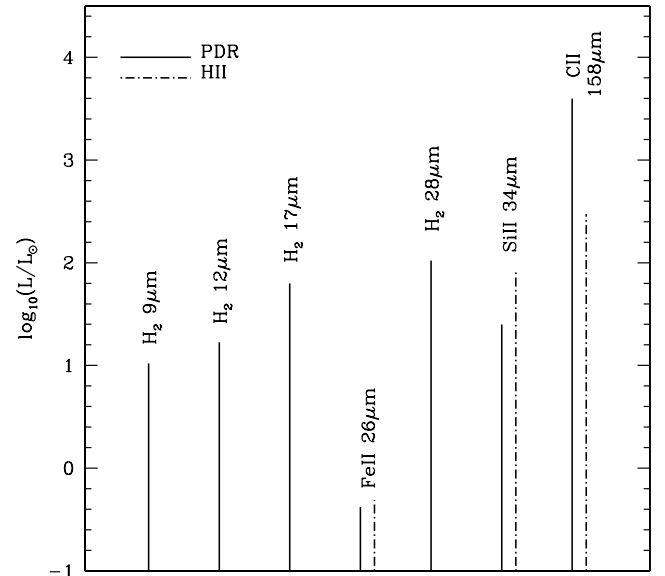

FIG. 19.—Luminosities of fine-structure and H$_2$ lines from H II region / PDR model with properties shown in Fig. 18 ($n_e = 10$ cm^{-3}, $\Phi_i = 10^{49}$ s^{-1}).

the H II region and PDR, we have computed a posteriori the fine-structure emission expected if n_H and n_e increased so as to maintain constant thermal pressure in the transition zone (see Fig. 18). The transition zone has a column density $\sim 10^{19}$ cm^{-2}, which, including the increase in gas density, corresponds to a length scale $\sim 10^{18}$ cm for the case presented here. This zone may contain up to $\sim 10\%$ of the mass in the H II region. For [C II] line emission, which arises from the upper state with lowest energy, the calculations show that including this region may increase the [C II] emission from the H II region up to 20%. The effect is smaller for [Si II] and [Fe II] since these have larger upper state energies and much of the gas in the transition region is too cool for efficient excitation of the lines. We do not include this contribution in the results presented below.

3.2. Parameter Study

Eight H II region/PDR models were constructed using standard abundances ($Z = 1$), with the initial conditions determined by the H II region. An additional eight models were produced using high metallicity, $Z = 3$. The number of ionizing photons was 10^{49} or 10^{51} s^{-1}, and these illuminated gas with electron densities of 1, 10, 100, and 10^3 cm^{-3}. Computed nebular temperatures for $Z = 1$ varied from ~ 7000 to ~ 9000 K, so pressure in the H II regions varied primarily with n_e. For a given cluster spectrum, higher density nebular gas results in a smaller value of R_S and therefore a higher value of FUV flux on the PDR surface:

$$G_0 \propto L_{\rm FUV}/R_S^2 \propto \Phi_i^{1/3} n_e^{4/3}. \qquad (1)$$

We use in deriving this correlation the fact that, for a given cluster mass distribution and age, Φ_i and $L_{\rm FUV}$ are proportional. The resulting values of G_0 range over four decades in the detailed calculations, from ~ 4 to $\sim 6 \times 10^4$. To match the nebular pressures, these require H nuclei densities in the PDR ranging from ~ 150 cm^{-3} for the low electron density (low G_0) cases to $\sim 2.5 \times 10^4$ cm^{-3} for the high electron density (high G_0) cases. Equilibrium temperatures at the PDR surface range from ~ 50 to 10^3 K, again increasing strongly with n_e and only weakly dependent on Φ_i.

In order to be able to interpret observations from high-metallicity systems, we have run eight additional models with gas-phase metal, dust, and PAH abundances increased by 3 over our standard values. In general, higher metal abundances lead to stronger metal line cooling and thus cooler nebular temperatures ($T \sim 3500-7500$ K). The increased dust abundance results in higher extinction for a given electron density and thus a proportionally smaller Strömgren radius.

The results for the relative contributions to [C II], [Si II], and [Fe II] emission from H II regions and PDRs for normal metallicity are summarized in Figure 20. First note that over the parameter space covered in these calculations, [C II] 158 μm emission is dominated by the PDRs surrounding H II regions. This result is similar to that shown by Carral et al. (1994), who found that PDRs dominated the [C II] emission, except for the case $n_e \leq 10$ cm^{-3}, where the contributions were about equal; we note, however, that the results they presented were based on simple arguments about the abundance of C$^+$ in the H II region at these low electron densities rather than a detailed calculation. Our results, based on self-consistent calculations of the nebular ionization structure down to electron densities as low as 1 cm^{-3}, indicate that PDRs contribute more than 90% of the [C II] emission for solar metallicity and the spectrum we have adopted. For all of the cases using our standard Starburst99 spectrum and with $Z = 1$, the ratio $L_{\rm C\,II}(\rm PDR)/L_{\rm C\,II}(\rm H\,II) \sim 10-20$, whereas Carral
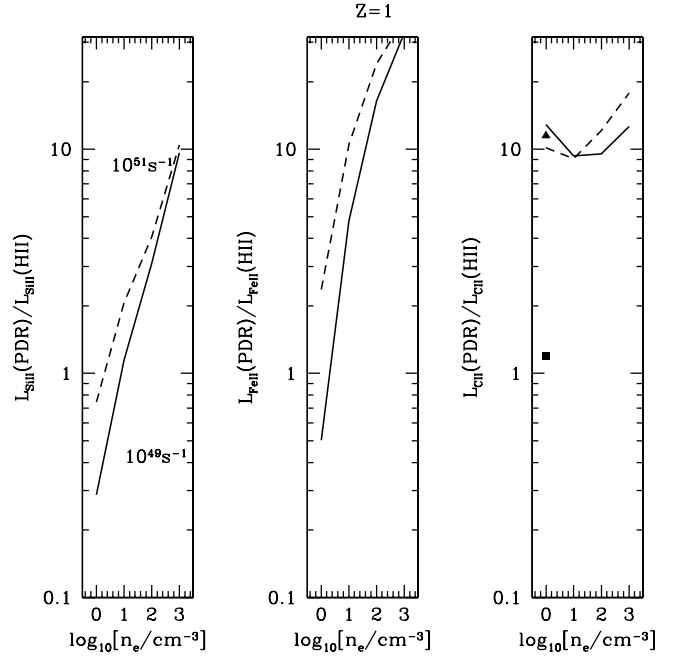

FIG. 20.—Relative contributions of PDRs and H II regions to [Si II], [Fe II], and [C II] fine-structure emission. Shown are our standard model results for $\Phi_i = 10^{49}$ (*solid lines*) and 10^{51} s^{-1} (*dashed lines*). In the [C II] panel, the triangle shows the result for the standard star cluster but for an age of only 10^6 yr. The square shows the result for the case where the cluster spectrum is a blackbody. See § 3.2 for details.

et al. (1994) found values of $\sim 5-20$ for $n_e \gtrsim 100$ cm^{-3} when they performed similar detailed calculations. Part of the difference results from a change in the electron excitation rate for [C II] (Blum & Pradhan 1992), which is a factor of ~ 2 lower than an older value adopted in Carral et al. (1994). In Figure 20 we also show results for two additional cluster spectra with $\Phi_i = 10^{49}$ s^{-1}. In one of the cases, we considered a cluster with an age of only 10^6 yr, so that some of the most massive stars are still contributing to the EUV spectrum. In this case, we still get a ratio $L_{\rm C\,II}(\rm PDR)/L_{\rm C\,II}(\rm H\,II) \sim 10$. We also consider the extreme case of a blackbody cluster spectrum, so that there is no break at the Lyman limit. Even in this case, where the ratio of EUV to FUV is much higher than would be expected for a real cluster, there is still more [C II] emission from the PDR than from the H II region. Thus, our result that PDRs dominate [C II] emission compared with their associated H II regions is robust even to extreme changes in the star cluster properties and even at very low H II region/PDR densities (see Fig. 20).

The Appendix presents an analytical analysis of the [C II] emission from H II regions and PDRs. We include this detailed analysis because it is extremely important to understand the origin of the [C II] line in galaxies since it is often the strongest line and potentially a powerful diagnostic of gas physical conditions.

For the high-metallicity cases, the ratio of PDR to H II region emission is generally lower. To first order, if the Strömgren radius were held fixed, an increase in the abundances in the H II region would lead to proportionally increased emission in the metal lines. In the PDR, as previously mentioned, the column of warm C$^+$ stays constant: the C$^+$ local abundance varies with Z, but the warm H column decreases with Z^{-1} because of enhanced dust extinction. Therefore, the [C II] intensity from the PDR should be relatively constant with Z. In practice, the variation is somewhat more complicated because of the interplay between
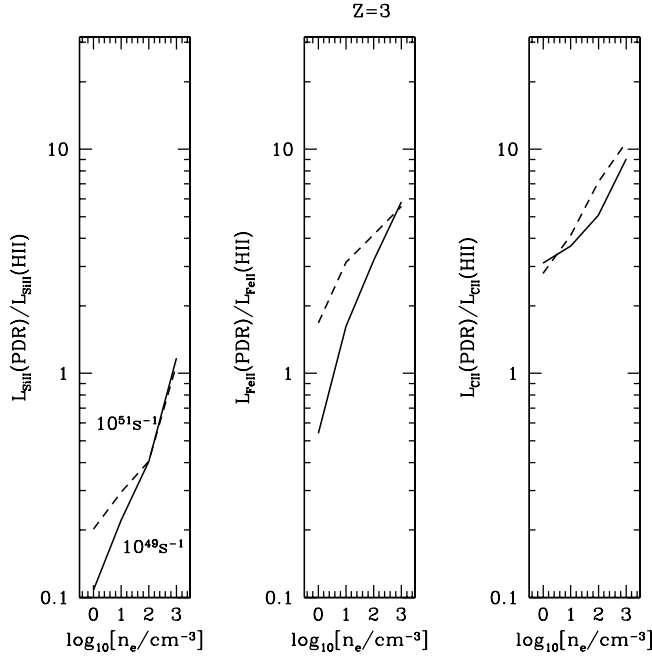
FIG. 21.—Relative contributions of PDRs and H ɪɪ regions to [Si ɪɪ], [Fe ɪɪ], and [C ɪɪ] fine-structure emission for metal abundances 3 times those in the local diffuse ISM ($Z = 3$). Shown are our model results for $\Phi_i = 10^{49}$ (*solid lines*) and 10^{51} s⁻¹ (*dashed lines*).

the H ɪɪ region and PDR conditions, with the largest differences for the low electron density cases. For $n_e = 1$ cm⁻³ and $\Phi_i = 10^{51}$ s⁻¹, the increased dust abundance means a ∼40% decrease in R_S as the EUV dust extinction becomes considerable. The effect of the decrease in R_S almost precisely balances the increase in gas abundance so that the [C ɪɪ] emission from the H ɪɪ region remains essentially the same. Since [C ɪɪ] emission dominates the PDR cooling at low densities, the PDR luminosity in this line is proportional to $\epsilon_{pe}G_0R_S^2$, where ϵ_{pe} is the efficiency of photoelectric heating. In this particular case, G_0 increases because of the smaller value of R_S, but the product $G_0R_S^2$ decreases because of the extra extinction from the H ɪɪ region (i.e., smaller R_S) in the high-metallicity case. In addition, the gas heating efficiency at the somewhat higher value of G_0 is about a factor of 2 lower than in the $Z = 1$ case. As a result, the [C ɪɪ] emission from the PDR is about 3 times smaller than in the standard case, and the ratio $L_{C ɪɪ}$(PDR)/$L_{C ɪɪ}$(H ɪɪ) drops to a value of ∼3 as shown in Figure 21.

The behavior of the [Si ɪɪ] and [Fe ɪɪ] ratios is somewhat more straightforward to understand since neither of these species dominates the cooling in the H ɪɪ region or the PDR. The densities in the PDRs and H ɪɪ regions modeled here are below the critical densities for both transitions. However, a larger fraction of Si is singly ionized in the H ɪɪ region than the fraction of Fe that is singly ionized. As a result, the H ɪɪ region produces proportionally less Fe ɪɪ emission than Si ɪɪ emission compared with the emission from PDRs. Thus, [Fe ɪɪ] emission is dominated by the PDR in all but one model, while [Si ɪɪ] emission may be dominated by the PDR or the H ɪɪ region.

3.3. *Comparison with Abel et al. (2005)*

After submission of this paper, the referee made us aware of a recently published paper, Abel et al. (2005). The authors have made similar calculations to those described here, using the CLOUDY (Ferland et al. 1998) photoionization model modified so as to also calculate the structure of, and emission from, neutral

PDR gas adjoining H ɪɪ regions. There are significant differences between the approaches of the two papers, but it is instructive to compare their results with those presented here. In particular, they also present results for the relative amounts of [C ɪɪ] and [Si ɪɪ] emission arising from H ɪɪ regions and PDRs.

Abel et al. (2005) explore the effect of varying the effective temperature of the star responsible for the H ɪɪ region, while we use a cluster of early-type stars as our illuminating source. Their approach is clearly more reasonable in moderate-sized stellar clusters where a single O star dominates the spectrum across the FUV and EUV. In very massive clusters, however, the spectrum results from an admixture of stellar spectra. We have compared our standard cluster spectrum with the atmosphere calculations presented in Sternberg et al. (2003) and find that it is similar in overall shape and strength of breaks to stars with $T_{\rm eff} \sim 40,000$ K and surface gravity $g = 10^4$ cm s⁻². We thus compare our results with the 42,000 K plots presented by Abel et al. (2005). Their plots give the percentage of line emission arising from the H ɪɪ region as a function of the ionized hydrogen density and the dimensionless ionization parameter $U = \Phi_i/4\pi R_S^2 n_e c \propto G_0/n_e$. Our model calculations extend to an H ɪɪ region density $n_e = 1$ cm⁻³, an order of magnitude lower than that presented by Abel et al. (2005), so there is no direct comparison there. At higher densities, our results correspond to points in their parameter space above and left of the line ($\log U, \log n_H$) = (−2.5, 1.0) to (−1.0, 3.0), in other words the upper left corner of each of their Figures 16–33.

For [C ɪɪ] and [Si ɪɪ], we can make a point-by-point comparison between our normal metallicity results and those in their Figures 32 and 33 for $T_{\rm eff} = 42,000$ K. The biggest difference for [C ɪɪ] occurs in their low-density case $n_e = 10$ cm⁻³ with $\Phi_i = 10^{49}$ photons s⁻¹, where we predict that ∼10% of the [C ɪɪ] emission is from the H ɪɪ region compared with their ∼25%. Although there is more than a factor of 2 difference, the PDR still is expected to dominate the emission. This difference may be understood as arising from different assumed gas-phase carbon abundances: Abel et al. (2005) use C/H = 3×10^{-4}, a factor of ∼2 larger than the value we adopted.

Our analytic result for the low-density limit in the Appendix (eq. [A9]) shows that the H ɪɪ region contribution scales with the metal abundance, so this difference is expected. For all of the other cases, the differences in our results are only a few percent, as expected since in the higher density case (eq. [A4]) the ratio is insensitive to the carbon abundance. For [Si ɪɪ], we find a factor of 2 less contribution from the H ɪɪ region for cases with electron density ≲10² cm⁻³, while agreement is excellent for $n_e = 10^3$ cm⁻³. Again, Abel et al. (2005) use a gas-phase silicon abundance Si/H = 4×10^{-6}, a factor of ∼2 larger than our standard value. [Si ɪɪ] emission from the H ɪɪ region scales with the silicon abundance at low density ($n_e \lesssim 10^3$ cm⁻³), while the situation is somewhat more complicated for the PDR. Our detailed calculations show that the [Si ɪɪ] emission from the PDR drops slightly for the same cluster conditions but with higher metallicity (including higher silicon and dust abundance) as the Strömgren radius is smaller and the pressure at the interface is lower. Both of these results serve to emphasize the sensitivity of low-density results to the assumed abundances. This is particularly important for our results that extend down to $n_e = 1$ cm⁻³, corresponding to ionized gas adjoining diffuse neutral gas.

4. DISCUSSION AND SAMPLE APPLICATIONS

On previous occasions, we have used our PDR models (e.g., Wolfire et al. 1990; K99; Malhotra et al. 2001; Hunter et al. 2001) combined with observations of [O ɪ], [C ɪɪ], and far-infrared dust emission to constrain the properties of PDRs. The technique

is to use emission-line ratios and the line-to-bolometric far-infrared continuum ratio to constrain G_0 and n. In this section we compare the results of this technique with those determined from the new H II region/PDR model and the predicted [Si II], [Fe II], and H_2 emission. By comparing predicted and observed line intensities, we are able to determine the gas density n, the incident FUV flux G_0, the filling factors of the emitting gas, and the abundances of Si^+ and Fe^+. We also discuss problems in using the [C II]/[O I] technique and the need to invoke simple and plausible two-component models as a way to simultaneously model the fine-structure and H_2 emission.

4.1. Application to the NGC 2023 Reflection Nebula

NGC 2023 is a well-studied reflection nebula northeast of the Orion Nebula and represents a relatively simple case for the study of PDR physics. A single B1.5 V star, HD 37903, produces a small region of ionized gas and illuminates a shell of molecular gas, producing characteristic PDR emission. Recent studies of the nebula include measurements of the intensities of [C II], [O I], and the far-infrared continuum (Howe et al. 1991; Steiman-Cameron et al. 1997), a large number of near-infrared H_2 rovibrational transitions (Burton et al. 1998), H_2 pure rotational transitions (Draine & Bertoldi 2000), and the [Si II] 35 μm fine-structure line (ISO archive). High-resolution imaging in the H_2 1–0 $S(1)$ line (e.g., McCartney et al. 1999) shows bright filamentary emission $\sim 1'$ south of HD 37903. Here we apply our models to this emission, which was also modeled by Draine & Bertoldi (2000).

Steiman-Cameron et al. (1997) presented [C II], [O I], and FIR continuum measurements at 14 positions in NGC 2023. Position H5 of that paper is centered on the filamentary H_2 1–0 $S(1)$ emission peak of McCartney et al. (1999). The ratio of coolant lines [O I] 63 μm/[C II] 158 μm = 5.4 at that position, and the line-to-bolometric FIR continuum ratio ([C II] 158 μm + [O I] 63 μm)/ FIR = 6.3×10^{-3}. Using the technique for comparing these ratios from K99, we find PDR parameters $G_0 = 3.5 \times 10^3$ and $n = 10^4$ cm^{-3}. However, the clumpy nature of the emission seen in the H_2 maps, as well as the analysis of Steiman-Cameron et al. (1997) showing that the [C II] emission must arise largely from the lower density gas surrounding the filaments, argues that we should be careful in treating the [C II] and [O I] emission as arising from the same gas. Thus, we follow Steiman-Cameron et al. (1997) and separate the emission into two components. Steiman-Cameron et al. (1997) showed that the emission could be understood as arising from a dense component ($n \sim 10^5$ cm^{-3}) filling 10% of the beam, while a lower density ($n \sim 10^3$ cm^{-3}) component filled the rest of the beam. Both components see an FUV field $G_0 \sim 3 \times 10^3$. We have repeated their analysis using the results of the K99 models and find that we get an excellent match to observations with the same densities and FUV field but with 20% of the emission coming from dense gas. With these parameters, 75% of the [O I] emission comes from the dense component since [O I] is the primary gas coolant at high density. On the other hand, nearly 75% of the [C II] emission comes from the lower density component: [C II] emission is insensitive to density above $n \sim 10^3$ cm^{-3}, so the contributions are approximately in the ratio of the component filling factors.

As a separate confirmation that the high-density component has the properties given above, we consider the H_2 emission observed with ISO by Draine & Bertoldi (2000) for the same position. Draine & Bertoldi (2000) presented H_2 column densities for rotational levels within the ground vibrational state, deduced from ISO observations of NGC 2023 for the $j = 2, 3, 4, 5, 6, 7, 9,$ and 15 levels. They multiplied the observed columns by a fac-

tor of 1.8 to account for beam dilution and multiplied the calculated (face-on) columns by a factor of 5 to account for the likely edge-on geometry. They found a good fit to the data for an FUV field $G_0 = 5 \times 10^3$ and density $n = 5 \times 10^4$ cm^{-3} and predict a (face-on) [Si II] 35 μm intensity of 3.0×10^{-4} ergs s^{-1} cm^{-2} sr^{-1}.

We find that we can match the ratios of measured column densities with $G_0 = 1 \times 10^4$ and $n = 5 \times 10^4$ cm^{-3} to better than 40% for j up to 15. In order to match the absolute column densities while using a filling factor of 20% for dense gas, as in our fine-structure analysis above, we find that we must allow for the dense gas to extend back along the line of sight by a factor of 6, so that the H_2 emission is essentially limb brightened by this factor. This is reasonable considering the edge-on shell-like geometry of the dense filaments seen in the McCartney et al. (1999) observations and is very close to the factor of 5 assumed by Draine & Bertoldi (2000). With $G_0 = 1 \times 10^4$, $n = 5 \times 10^4$ cm^{-3}, and a dense component filling factor of 20%, we get the same [O I] intensity in the analysis above because the [O I] line is optically thick, so that the additional factor of 6 of PDR column does not raise the [O I] intensity by an appreciable amount. However, our [C II] is much less than observed, so we need a lower density interclump medium as before.

Our merged H II region/PDR model with 10^{49} ionizing photons s^{-1} and an ionized gas density $n_e \sim 100$ cm^{-3} has conditions $G_0 \sim 3 \times 10^3$ and $n \sim 10^4$ cm^{-3}, comparable to those found in the [O I] and [C II] analysis. Thus, the model serves as a useful guide in determining the contributions of H II region and PDR gas to atomic fine-structure emission. The merged model predicts that essentially all of the [C II] and [Fe II] emission is from the PDR, while $\sim 60\%$ of [Si II] comes from the PDR. Because HD 37903 is a B1.5 V star, it is less luminous in the EUV than our model; therefore, the simple model overestimates the H II region contribution. Our determination of G_0 and n ignored the contribution of ionized gas to [C II] emission, but this assumption appears to be justified given that $L_{C II}(PDR)/L_{C II}(H II) \gtrsim 10$.

[Si II] 35 μm emission has also been observed in NGC 2023. From the ISO archive, we have extracted a line intensity of $\sim 10^{-5}$ ergs s^{-1} cm^{-2} sr^{-1}. Our merged PDR/H II region model predicts that at least 60% of that emission comes from the PDR, and for the PDR conditions determined above the predicted [Si II] intensity is $\sim 6 \times 10^{-5}$ ergs s^{-1} cm^{-2} sr^{-1}. In order to match the observations, the gas-phase Si abundance in NGC 2023 must be at least 6 times smaller than what we assume in our models, depending on a more exact treatment of the H II region produced by the B1.5 V star. Comparing the predicted and observed [Si II] intensities would then indicate rather low values of the gas-phase silicon abundance ($\lesssim 2.5 \times 10^{-7}$; see Table 1). Note that Draine & Bertoldi (2000) also overpredict the [Si II] intensity, again indicating substantially lower gas-phase Si abundances than assumed in the model.

4.2. [C II] Emission from the Inner Galaxy

The total luminosity of [C II] from the Galaxy as a whole as measured by the COBE satellite is $\sim 5 \times 10^7$ $L_\odot$ (Wright et al. 1991). The dominant origin of this emission as a function of position in the Galaxy is uncertain due to line-of-sight confusion and due to the various ISM components that can produce [C II] emission. The emission may arise from the cold ($T \sim 100$ K) diffuse neutral gas (Bennett et al. 1994), molecular cloud surfaces illuminated by the interstellar radiation field (Shibai et al. 1991), or the diffuse low-density ionized gas (Heiles 1994). The contribution from high-density H II is unlikely to be significant when averaged over the $7°$ COBE beam.

Based in part on the theoretical ratio of [N II] 205 μm to [C II] 158 μm emission, Heiles (1994) argued that most of the [C II] from the inner Galaxy observed in the *COBE* beam must arise from the diffuse low-density ionized gas. We have calculated the expected ratio based on updated collision strengths and new measurements of the relative abundances of nitrogen and carbon (Sofia et al. 2004; Meyer et al. 1997) and find that $\gtrsim$50% of the [C II] emission arises from neutral gas exposed to FUV radiation (M. G. Wolfire et al. 2006, in preparation).

The inner Galaxy probed by these observations shows evidence for metal abundances $\sim$2–3 times the values in the local diffuse ISM (e.g., Shaver et al. 1983). Thus, our $Z = 3$ models are appropriate here. In Figure 21 we show that at low density, roughly 75% of [C II] emission is expected to arise from neutral gas, if our standard spectrum approximates the spectra in the Galactic center. Note, however, that the results are not sensitive to the spectra, except in the unlikely case of blackbody spectra (i.e., no jump at the Lyman limit). This calculation, however, assumes that the neutral gas extends to $A_V \sim 10$ in all directions around the FUV source so that all of the FUV photons are converted with an efficiency of order 1% into [C II] 158 μm photons. If, however, a significant fraction of the FUV escapes the Galactic plane, then the ratio $L_{\rm C\,II}({\rm PDR})/L_{\rm C\,II}({\rm H\,II})$ drops. In the inner disk, the average vertical column density from the midplane outward is $\sim$$3 \times 10^{20}$ cm^{-2}, corresponding to $\sim$0.6 mag of extinction in the FUV for $Z = 3$. As a result, roughly half of the FUV photons produced in the inner Galaxy can escape. Thus, we expect that roughly 50% of the [C II] emission from the inner Galaxy will be produced in neutral gas.

4.3. *Application to NGC 7331*

As an example of the application of our models to an extragalactic source, we discuss here results from Spitzer Infrared Nearby Galaxies Survey (SINGS) Legacy observations of the normal spiral galaxy NGC 7331, previously examined in an early release paper by Smith et al. (2004). Here we focus primarily on several infrared tracers of PDRs and H II regions observed in the nucleus and the associated circumnuclear ring, regions of NGC 7331 observed with *Spitzer* and *ISO*. The ultraviolet spectrum from the exciting sources in NGC 7331 should be closer to the situations we have modeled than NGC 2023; for NGC 2023 a single B star dominates the UV spectra, but in NGC 7331 there are certainly massive stellar clusters providing the UV, as is assumed in our model Starburst99 spectra.

NGC 7331 is a quiescent Sb-type galaxy (Smith et al. 2004) with a moderate ratio of infrared to visible luminosities. Measurements of nebular lines of [O II] and [O III] indicate that metal abundances in the inner disk and nucleus of NGC 7331 are as much as 3 times solar (Oey & Kennicutt 1993), similar to that found in the Galactic center. In order to model the emission from NGC 7331, we use our $Z = 3$ PDR/H II region models.

We have computed [Si II] and [Fe II] intensities for PDR regions with $Z = 3$. The computed intensities are generally larger than those shown in Figures 1 and 2 since, as noted above, the PDR temperature is higher than at normal metallicity.[8] The exact increase in intensity depends on both the column of each species and the temperature in the fine-structure line-emitting region. The intensity of [C II] emission is not as affected by the increased abundance since it is the dominant coolant of the gas over much of the parameter space and it is insensitive to changes in temperature above about 92 K. The gas temperature adjusts so that

[C II] emission continues to cool the gas with the efficiency controlled by the ratio G_0/n_e, where n_e in the PDR is a function of the metallicity. For the H₂ lines, the intensities increase with Z at a given (n, G_0) combination since the increased dust abundance leads to a higher H₂ formation rate and therefore larger column of warm H₂. H₂ line intensities and line ratios for $Z = 3$ are shown in Figures 12–15.

We begin by examining the observed H₂ emission, seen in the lowest three pure rotational transitions, 0–0 $S(0)$ 28 μm, 0–0 $S(1)$ 17 μm, and 0–0 $S(2)$ 12 μm, which are only excited in warm molecular gas, presumably in regions adjacent to H II regions. We have compared the observed emission-line ratios to the results presented in Figures 12, 13, and 14. The H₂ line ratios for $Z = 3$ imply that the emission is coming from regions with molecular gas density $n \sim 1.5 \times 10^4$ cm^{-3} and FUV fields $G_0 = 250$ times the average interstellar value. Malhotra et al. (2001) found that somewhat lower values of density, but similar G_0, were necessary to explain the ratios of [C II] and [O I] fine-structure lines, as well as the line-to-continuum ratio, from a large sample of nearby normal galaxy disks. The result was interpreted to mean that the integrated fine-structure emission from normal galaxies is dominated by gas associated with dense star-forming regions. These H₂ results seem to imply even denser gas in the NGC 7331 nuclear star-forming regions. Since the molecular hydrogen line ratios constrain the gas density and FUV field, we may then use the ratio of predicted-to-observed absolute line intensities to estimate the area filling factor of H₂-emitting gas. In the case of all three lines, the predicted intensity is 2.9 times the observed intensity. If the line ratio analysis is correct, then the surface area of H₂-emitting gas is about $\frac{1}{3}$ of the *Spitzer* beam projected area. Note that if the PDRs around molecular clouds are spherical shells (or randomly oriented), then they may only fill $\sim$1/12 of the beam since their total surface area is $\sim$4 times their projected surface area.

J. Brauher (2005, private communication) has compiled *ISO* observations of [O I] and [C II] intensities and total infrared continuum from a $\sim$90$''$ *ISO* beam with the same beam center as the *Spitzer* H₂ observations. We applied our standard method to independently derive values of G_0 and n. The observed ratios are [O I]/[C II] = 0.5 and ([O I] + [C II])/FIR = 3×10^{-3}. For our $Z = 3$ models, there is only one solution that matches the observed ratios, $n \sim 10^4$ cm^{-3} and $G_0 \sim 1$. However, the absolute intensities of the [O I] and [C II] lines predicted by the models for these conditions are so low that the observed line intensities require beam filling factors of several hundred. This is especially unlikely for the [O I] line, which is (marginally) optically thick from a single PDR cloud, and strong [O I] emission only arises from dense, warm PDRs. If most of the [O I] emission arises from warm, dense PDRs, while most of the [C II] emission is emitted by lower density gas, then the ratios we measure represent an ensemble average that does not match the conditions in either component.

The [O I] 63 μm intensity measured by Brauher is 2.1×10^{-5} ergs s^{-1} cm^{-2} sr^{-1} averaged over the $\sim$90$''$ *ISO* beam, while our model for the conditions given by the H₂ lines predicts an intensity $\sim$$2 \times 10^{-3}$ ergs s^{-1} cm^{-2} sr^{-1}, requiring that the [O I] emission fill only about 1% of the beam, some 8–30 times less than the H₂. The sum of H₂ rotational line emission in $S(0)$, $S(1)$, and $S(2)$ measured by Smith et al. (2004) is also about 10^{-5} ergs s^{-1} cm^{-2} sr^{-1}, but this was averaged over a *Spitzer* beam $\sim$10 times smaller than that of *ISO* at 63 μm. Smith et al. (2004) also give an intensity for the $S(0)$ line over a significantly larger area weighted toward the molecular ring outside the nucleus of NGC 7331, while $S(1)$ and $S(2)$ lines are not detected,

---

[8] Figures for $Z = 3$ may be found at the PDR Toolbox located at http://dustem.astro.umd.edu.

<div align="center">TABLE 3</div>
<div align="center">Model of NGC 7331</div>

Parameter	Symbol	Value
FUV field at dense cloud surfaces	$G_{0,\mathrm{dense}}$	250
Density of neutral gas at dense cloud surfaces..............................	n_{dense}	1.5×10^4 cm^{-3}
Fraction of FUV luminosity shining on dense gas.........................	η_{dense}	0.2
Fraction of FUV luminosity shining on diffuse gas........................	η_{diff}	0.8
Efficiency of [C II] emission from dense PDRs.............................	$\epsilon_{\mathrm{C\,II,\,dense}}$	3.75×10^{-3}
Efficiency of [C II] emission from diffuse PDRs	$\epsilon_{\mathrm{C\,II,diff}}$	2.5×10^{-2}
Ratio of [C II] from H II to PDR, dense	$[L_{\mathrm{C\,II}}(\mathrm{H\,II})/L_{\mathrm{C\,II}}(\mathrm{PDR})]_{\mathrm{dense}}$	0.20
Ratio of [C II] from H II to PDR, diffuse......................................	$[L_{\mathrm{C\,II}}(\mathrm{H\,II})/L_{\mathrm{C\,II}}(\mathrm{PDR})]_{\mathrm{diff}}$	0.33
Fraction of diffuse FUV field absorbed in the galaxy.....................	f_{diff}	0.30
FUV luminosity	L_{FUV}	$5 \times 10^9\ L_\odot$
Luminosity of [C II], dense medium	$L_{\mathrm{C\,II}}(\mathrm{dense})$	$4.5 \times 10^6\ L_\odot$
Luminosity of [C II], diffuse medium	$L_{\mathrm{C\,II}}(\mathrm{diff})$	$4.0 \times 10^7\ L_\odot$
Ratio of [C II] from diffuse and dense ISM..................................	$L_{\mathrm{C\,II}}(\mathrm{diff})/L_{\mathrm{C\,II}}(\mathrm{dense})$	~ 9

indicating that the extranuclear gas is cooler and/or lower density and thus not likely to produce substantial [O I] emission. If we assume that all of the [O I] emission measured with *ISO* actually arises from the same nuclear gas as the H$_2$ emission, then the [O I] intensity within the *Spitzer* beam is $\sim 2 \times 10^{-4}$ ergs s^{-1} cm^{-2} sr^{-1}, requiring a beam filling factor of 10%, which matches the H$_2$ results if the emission comes from the surfaces of three-dimensional ("spherical") clouds. The H$_2$ emission is optically thin and therefore would reach the beam from all sides of a spherical cloud, while optically thick [O I] emission would come only from the face closest to the observer. Thus, it appears that both [O I] and H$_2$ are well explained by clouds in the nucleus with a projected area filling factor of $\sim 10\%$.

While the emission from dense gas tracers is explained by our scenario above, the fact that strong [C II] emission is observed means that at least some emission arises in diffuse gas where [C II] is the dominant gas coolant. We consider a "blister" model in which OB associations shine on the edges of clouds in the nucleus of NGC 7331. In this model, a fraction η_{dense} of the total cluster FUV luminosity is intercepted by the dense cloud, while a fraction $\eta_{\mathrm{diff}} = 1 - \eta_{\mathrm{dense}}$ escapes to the diffuse medium. The [C II] luminosity of the dense medium is

$$L_{\mathrm{C\,II,dense}} = \eta_{\mathrm{dense}} \left\{ 1 + [L_{\mathrm{C\,II}}(\mathrm{H\,II})/L_{\mathrm{C\,II}}(\mathrm{PDR})]_{\mathrm{dense}} \right\} \\ \times \epsilon_{\mathrm{C\,II,\,dense}} L_{\mathrm{FUV}}, \tag{2}$$

where the term in square brackets accounts for the contribution to [C II] emission from dense ionized gas and $\epsilon_{\mathrm{C\,II,dense}}$ is the efficiency with which PDR heating is converted to [C II] emission in the dense PDR gas. The [C II] luminosity of the diffuse medium is

$$L_{\mathrm{C\,II,diff}} = \eta_{\mathrm{diff}} \left\{ 1 + [L_{\mathrm{C\,II}}(\mathrm{H\,II})/L_{\mathrm{C\,II}}(\mathrm{PDR})]_{\mathrm{diff}} \right\} \\ \times \epsilon_{\mathrm{C\,II,diff}} f_{\mathrm{diff}} L_{\mathrm{FUV}}, \tag{3}$$

where the term in square brackets accounts for the contribution to [C II] emission from diffuse ionized gas, $\epsilon_{\mathrm{C\,II,diff}}$ is the efficiency with which PDR heating is converted to C II line emission in the diffuse PDR gas, and f_{diff} is the fraction of FUV reaching the diffuse medium that is actually absorbed by diffuse gas without escaping the galaxy.

Detailed calculations by Parravano et al. (2003) indicate that, averaged over the ~ 30 Myr massive cluster lifetime, a fraction $\eta_{\mathrm{dense}} \sim 20\%$ of the FUV photons produced by massive stars end up illuminating nearby dense molecular clouds, while $\eta_{\mathrm{diff}} \sim 80\%$ reaches the diffuse ISM. The 20% of the FUV photons that are intercepted by the nearby molecular gas provide conditions similar to those found from H$_2$: $G_0 \sim 250$ and $n \sim 1.5 \times 10^4$ cm^{-3}. Under these conditions with $Z = 3$, we find that most dust grains in the PDR gas are neutral and the photoelectric heating efficiency is near the maximum of $\sim 2.5\%$, with most of the line emission emerging as [O I] at these high densities. Only $\sim 15\%$ of the line cooling is in the [C II] line, so $\epsilon_{\mathrm{C\,II,\,dense}} = 0.15 \times 0.025 = 3.75 \times 10^{-3}$. Under the same conditions, our combined H II region/PDR model shows that an additional 20% must be added to the [C II] emission to account for the contribution from dense H II gas. On the other hand, the FUV photons that reach the diffuse medium shine on neutral gas with low FUV field and low density. Again under these conditions, the dust grains are primarily neutral and the efficiency of photoelectric heating is also $\sim 2.5\%$, here emerging almost entirely as [C II] emission (i.e., [O I] is weak). According to our H II region/PDR model, $\sim 75\%$ of the [C II] emission must come from the diffuse PDR clouds and only $\sim 25\%$ from the low-density H II regions, so an additional 33% must be added to the [C II] emission to account for the contribution from diffuse ionized gas. The model parameters are summarized in Table 3. Inserting these values into the expressions above gives

$$\frac{L_{\mathrm{C\,II}}(\mathrm{diff})}{L_{\mathrm{C\,II}}(\mathrm{dense})} = \frac{0.8(1 + 0.33)(0.025 f_{\mathrm{diff}})(0.025 L_{\mathrm{FUV}})}{0.2(1 + 0.20)(0.00375 L_{\mathrm{FUV}})} \tag{4}$$

$$\sim 27 f_{\mathrm{diff}}, \tag{5}$$

so that the diffuse component dominates the [C II] emission as long as $f_{\mathrm{diff}} \gtrsim 0.04$. We can compare the predicted [C II] luminosity in this model with the observed [C II] luminosity. The observed [C II] luminosity in the $\sim 90''$ *ISO* beam is $4.5 \times 10^7\ L_\odot$. To predict the [C II] emission, we use the observed [O I] luminosity ($L_{\mathrm{O\,I}} \sim 2 \times 10^7\ L_\odot$) to determine the total FUV luminosity. The [O I] luminosity is produced when the 20% of L_{FUV} shining on the dense gas is converted with an efficiency of 2.1% to [O I] line emission. Thus, the total FUV luminosity of the clusters is $L_{\mathrm{FUV}} = L_{\mathrm{O\,I}}/(0.2 \times 0.021) \sim 5 \times 10^9\ L_\odot$.[9] The 80% of L_{FUV} that illuminates diffuse gas gives $L_{\mathrm{C\,II}} = 1.3 \times 10^8 f_{\mathrm{UV}}\ L_\odot$, which matches the observed [C II] luminosity if $f_{\mathrm{diff}} \sim 0.30$, so that $L_{\mathrm{C\,II}}(\mathrm{diff})/L_{\mathrm{C\,II}}(\mathrm{dense}) \sim 9$. Thus, 70% of the FUV flux reaching the diffuse ISM penetrates and escapes the galaxy. However, the 30% that is absorbed in the diffuse ISM is sufficient to produce roughly 90% of the observed [C II] emission.

---

[9] The total infrared luminosity is $\sim 10^{10}\ L_\odot$, at least 50% of which comes from dust heating by photons less energetic than 6 eV, i.e., outside the FUV band.

The fine-structure emission seen in the *ISO* beam when viewing other galaxies is an admixture of emission from diffuse and dense gas. The key consequence of this fact is that we derive values for G_0 and n that do not represent either region when we use the [C II] and [O I] lines alone as diagnostics. [C II] tends to arise from the diffuse ISM, whereas [O I] arises from dense PDR surfaces of molecular clouds, similar to the H$_2$ emission. In this case, the H$_2$ emission gives a more appropriate sense of the star-forming conditions in the molecular clouds since little H$_2$ emission arises from the diffuse gas. Modeling using [O I] in galaxies is problematic since the line becomes optically thick more readily than [C II] and H$_2$ and so is more sensitive to the geometry and orientation of the dense PDRs.

The high densities and UV fields implied by the H$_2$ results can be matched with our H II/PDR models to give an estimate of the densities in the H II regions associated with the molecular gas. The pressure in the (PDR) molecular gas is of order 2.5×10^6 cm^{-3} K, so the H II regions ($T \sim 10^4$ K) must have densities $n_e \sim 10^2$ cm^{-3}, near the high end of the range we explored, and consistent with an upper limit determined by Smith et al. (2004) from [S III] line ratios. At these high densities (see Fig. 21) at least 80% of the [C II] emission from the dense component arises from the dense PDR, as opposed to the interior H II region.

[Fe II] and [Si II] emission is very weak from the diffuse ISM and certainly will be dominated by the dense component. [Fe II] will be of order 3 times stronger from the dense PDR than from the dense H II region, and [Si II] emission will be about 30% from the PDR, somewhat lower than what we found in NGC 2023. Smith et al. (2004) used *Spitzer* to observe the [Si II] and [Fe II] lines and found intensities of 5×10^{-5} and 4×10^{-6} ergs s^{-1} cm^{-2} sr^{-1}, respectively. The PDR model for the conditions inferred from the H$_2$ emission, including beam filling, predicts intensities of 5×10^{-5} and 1.3×10^{-6} ergs s^{-1} cm^{-2} sr^{-1} for the same lines. If, as the H II/PDR model implies, 30% of the Si II and 80% of the Fe II comes from the PDR, then we may estimate the abundances of these species based on the filling factor determined from the H$_2$ lines and the predicted intensities. Correcting for the H II region contribution to each line and assuming an area filling factor of $\sim$30% as found from the H$_2$ lines, we find that the gas-phase iron abundance must be $\sim 1.2 \times 10^{-6}$, $\sim$7 times the gas-phase abundance in the diffuse ISM of the Milky Way, and roughly twice what we assumed for the $Z = 3$ environment of this galaxy. On the other hand, gas-phase silicon is enhanced by a factor of $\sim$3 over its Milky Way diffuse ISM value, consistent with our $Z = 3$ model.

We note that the high FUV field implied by the H$_2$ observations should result in warm grains with $T \sim 40$ K that emit strongly in the mid-IR continuum. The dust spectral energy distribution (SED) observed by Regan et al. (2004) for NGC 7331 peaks at $\sim$100 μm, suggesting grains that are not as hot as expected if the SED arises due to the FUV field in the dense gas, $G_0 \sim 250$. If the ISM in the *Spitzer* beam is the mixture of diffuse gas ($G_0 \sim 1$) and dense gas ($G_0 \sim 250$) that we propose above, then the hot FIR emission from the H$_2$-emitting gas may be sufficiently beam diluted to not conflict with the observed continuum. More detailed modeling of the dust continuum spectrum is required, and a future paper will more carefully analyze NGC 7331 and other SINGS galaxies.

5. SUMMARY

We have presented the results of a model in which fine-structure emission from [C II], [Si II], and [Fe II] is produced from both H II regions and associated PDRs. The PDRs are also responsible for rovibrational and pure rotational emission from H$_2$. The model uses cluster spectra from Starburst99/Mappings as inputs for both a nebular emission model and a PDR model. For the assumed cluster properties, the model results show that [C II] emission is dominated by PDRs, whereas the [Si II] and [Fe II] emission may come from either region depending primarily on the gas density in the H II region. The H II region component becomes stronger in lower density, larger H II regions surrounded by PDRs and in higher metallicity environments. We show that H$_2$ pure rotational transitions can be used to probe the conditions in dense PDRs associated with star formation regions. We find that in probing conditions in external galaxies, where the telescope beam size is typically kiloparsecs across and encompasses an ensemble of molecular and diffuse clouds, the H$_2$ emission may be a good probe of the dense molecular cloud surfaces. [C II] tends to arise from the diffuse PDR clouds; [O I] arises from the dense molecular cloud surfaces, but this line readily becomes optically thick and so its intensity depends on geometry.

We apply our results to three regions. In the relatively simple case of the well-studied NGC 2023 reflection nebula, we find similar conditions using either the standard PDR tracers of [C II], [O I], and far-infrared continuum emission or the H$_2$ pure rotational transitions. By comparing the predicted and observed [Si II] emission, we infer a gas-phase silicon abundance $\sim$7 times smaller than that measured in diffuse clouds.

We apply our models of [C II] emission to *COBE* observations of [C II] from the Milky Way. We find that it is likely that the [C II] emission arises from diffuse PDR clouds (the cold neutral medium [CNM]), or PDRs surrounding or neighboring H II regions, but that diffuse H II regions likely contribute only 25%–50% of the emission.

We also compare our models with observations of the normal galaxy NGC 7331. Here the results from [C II], [O I], and continuum measurements give lower values for the PDR densities and incident FUV fields than the H$_2$ pure rotational transitions. We interpret this to mean that both diffuse and dense ISM falls in the telescope beams, and while H$_2$ and [O I] emission is dominated by dense PDRs, the [C II] emission arises primarily from diffuse clouds. The dense PDR surfaces of molecular clouds may contribute $\sim$20%–50% of the [C II] emission. This indicates that H$_2$ emission more accurately probes the conditions in dense gas and that caution must be used in interpreting the results from fine-structure tracers. We also show that the [Si II] and [Fe II] emission can be explained by our merged PDR/H II region model if the gas-phase abundances in the nucleus of NGC 7331 are enhanced by $\sim$3 for silicon and $\sim$7 for iron over the diffuse cloud values in the Galaxy. Since the metallicity may be $\sim$3 times solar in the nucleus of NGC 7331, this implies the same fractional depletion of silicon onto grains in this region as in the local ISM, whereas iron is somewhat less depleted in this region. Most of the [Si II] emission arises from H II regions, whereas most of the [Fe II] emission arises from PDRs.

APPENDIX

ANALYTICAL CALCULATION OF [C II] EMISSION FROM H II REGIONS AND PDRs

An analytical calculation shows that the PDR likely dominates the [C II] emission for ionization-bounded H II regions at solar metallicity. For an H II region without dust, the classic Strömgren radius calculation gives $R_S = 67(\Phi_{49}^{1/3}/n_e^{2/3})$ pc, where $\Phi_i = 10^{49}\Phi_{49}$ s^{-1}. The luminosity of the 158 μm line from the H II region is

$$L_{C\,II}(H\,II) = (4/3)\pi R_S^3 n_e Z x_C f_u(H\,II)A_{ul}\Delta E f_{C^+} \tag{A1}$$

$$= 1.45 \times 10^{38}(\Phi_{49}/n_e)Z f_u(H\,II)f_{C^+} \text{ ergs s}^{-1}, \tag{A2}$$

where Zx_C is the gas-phase carbon abundance, $f_u(H\,II)$ is the fraction of C$^+$ that is in the upper state of the 158 μm transition, A_{ul} is the Einstein A-value for the transition, ΔE is the energy difference between the upper and lower states, and f_{C^+} is the fraction of carbon that is singly ionized in the nebula. The upper energy level $\Delta E/k \sim 92$ K is well below the temperature in the H II regions, so the resulting value of f_u is not strongly dependent on the gas temperature. In this case the expression for f_u becomes $f_u(H\,II) = 2/[3 + (n_{e,cr}/n_e)]$, where the critical density for electron collisions to thermalize the upper energy level of this transition is $n_{e,cr} \sim 50$ cm^{-3}.

The [C II] luminosity from the PDR depends on the PDR surface area, the column density of C$^+$, and the temperature of the PDR gas when the gas is below about 92 K. However, for the models presented here, the temperature of the C II–emitting gas is below 92 K only for the $n_e = 1$ cm^{-3}, $\Phi_i = 10^{49}$ s^{-1} case. In PDRs, carbon remains mostly ionized to a hydrogen nucleus column $N_{max} \sim (10^{21}/Z)$ cm^{-2}, as long as shielding of FUV photons is dominated by dust rather than H$_2$ self-shielding (K99), a condition that holds in all of the PDR regions of the merged models considered in this paper. Thus,

$$L_{C\,II}(PDR) = 4\pi R_S^2 N_{max} Z x_C f_u(PDR)A_{ul}\Delta E, \tag{A3}$$

where $f_u(PDR)$ is the fraction of C$^+$ in the upper state in the PDR. Note that $L_{C\,II}(PDR)$ is independent of Z since $N_{max} \propto 1/Z$.

We now calculate $L_{C\,II}(PDR)/L_{C\,II}(H\,II)$ for both the low- and high-density limits. The critical density for collisions with H atoms is $n_{H,cr} \sim 3000$ cm^{-3}, and both the PDR temperature and density enter into $f_u(PDR)$. In the limit where both the H II region and PDR densities are above their respective critical densities (i.e., $n_e > 100$ cm^{-3} for the PDR density to be greater than $n_{H,cr}$) and the PDR gas has a temperature above 92 K from the surface to N_{max},

$$\frac{L_{C\,II}(PDR)}{L_{C\,II}(H\,II)}_{\text{high density}} = 15\frac{N_{21}}{Zn_e^{1/3}\Phi_{49}^{1/3}}\frac{1}{f_{C^+}}. \tag{A4}$$

Detailed calculations show that $f_{C^+} \sim 0.25$ and ~ 0.1 for $n_e = 10^3$ cm^{-3} with $\Phi_i = 10^{49}$ and 10^{51} s^{-1}, respectively. An additional correction needs to be applied to the analytic expression in the limit of high density since in this limit dust extinction significantly reduces the effective ionization rate and hence the Strömgren radius from the dust-free value. When these are taken into account, the agreement with the models is very good. For the case with $n_e = 10^3$ cm^{-3} and $\Phi_i = 10^{49}$ s^{-1}, the analytic result including the corrections gives a ratio of $\sim$27, while the model calculation gives $\sim$22; for $\Phi_i = 10^{51}$ s^{-1}, the analytic and model results are $\sim$22 and $\sim$18, respectively. All of the high-density cases predict approximately $\sim$15–20 times as much [C II] emission from the PDR as from the H II region for $Z = 1$ and the standard spectrum.

In the low-density limit, when both the H II region and PDR have densities below the critical densities for [C II], the emissivity of the [C II] line in the H II region is set by the rate of collisional excitation from the ground state:

$$L_{C\,II}(H\,II) = \frac{4}{3}\pi R_S^3 \gamma_e n_e n_{C^+}\Delta E, \tag{A5}$$

where $\gamma_e \sim 10^{-7}$ cm^3 s^{-1} is the collisional excitation rate with electrons at $T \sim 10^4$ K. Substituting for R_S in terms of Φ_i and n_e, we find

$$L_{C\,II}(H\,II) = 6 \times 10^{36}Z\Phi_{49}f_{C^+} \text{ ergs s}^{-1}. \tag{A6}$$

Detailed calculations at low density show that $f_{C^+} \sim 0.5$. We calculate the C II luminosity from the PDR by noting that at low densities the 158 μm line is the dominant gas coolant. The FUV luminosity of the model clusters $L_{FUV} = 3 \times 10^{39}\Phi_{49}$ ergs s^{-1}; for the PDR conditions in this case ($n_H \sim 10^2$ cm^{-3}, $G_0 \sim 10$) our model shows that FUV luminosity is converted to 158 μm line emission via photoelectric heating with an efficiency $\epsilon_{pe} \sim 2\%$ independent of Z. Thus,

$$L_{C\,II}(PDR) = 3 \times 10^{39}\Phi_{49}\epsilon_{pe} \text{ ergs s}^{-1} \tag{A7}$$

$$\sim 6 \times 10^{37}\Phi_{49} \text{ ergs s}^{-1}, \tag{A8}$$

giving a characteristic ratio

$$\frac{L_{C\,II}(PDR)}{L_{C\,II}(H\,II)}_{\text{low density}} \sim 10/Z. \tag{A9}$$

REFERENCES

Abel, N. P., Ferland, G. J., Shaw, G., & van Hoof, P. A. M. 2005, ApJS, 161, 65
Abgrall, H., Le Bourlot, J., Pineau Des Forets, G., Roueff, E., Flower, D. R., & Heck, L. 1992, A&A, 253, 525
Allers, K. N., Jaffe, D. T., Lacy, J. H., Draine, B. T., & Richter, M. J. 2005, ApJ, 630, 368
Bennett, C. L., et al. 1994, ApJ, 434, 587
Bergin, E. A., et al. 2000, ApJ, 539, L129
Black, J. H., & van Dishoeck, E. F. 1987, ApJ, 322, 412
Blum, R. D., & Pradhan, A. K. 1992, ApJS, 80, 425
Burton, M. G., Hollenbach, D. J., & Tielens, A. G. G. M. 1990, ApJ, 365, 620
———. 1992, ApJ, 399, 563
Burton, M. G., Howe, J. E., Geballe, T. R., & Brand, P. W. J. L. 1998, Publ. Astron. Soc. Australia, 15, 194
Carral, P., Hollenbach, D. J., Lord, S. D., Colgan, S. W. J., Haas, M. R., Rubin, R. H., & Erickson, E. F. 1994, ApJ, 423, 223
Draine, B. T., & Bertoldi, F. 1996, ApJ, 468, 269
———. 2000, in Molecular Hydrogen in Space, ed. F. Combes & G. Pineau des Forêts (Cambridge: Cambridge Univ. Press), 131
Ferland, G. J., Korista, K. T., Verner, D. A., Ferguson, J. W., Kingdon, J. B., & Werner, E. M. 1998, PASP, 110, 761
Flower, D. R., & Roueff, E. 1998, J. Phys. B, 31, L955
Habart, E., Boulanger, F., Verstraete, L., Walmsley, C. M., & Pineau des Forêts, G. 2004, A&A, 414, 531
Habing, H. J. 1968, Bull. Astron. Inst. Netherlands, 19, 421
Heidner, R. F., & Kasper, V. V. 1972, Chem. Phys. Lett., 15, 179
Heiles, C. 1994, ApJ, 436, 720
Hollenbach, D. J., Takahashi, T., & Tielens, A. G. G. M. 1991, ApJ, 377, 192
Howe, J. E., Jaffe, D. T., Genzel, R., & Stacey, G. J. 1991, ApJ, 373, 158
Hunter, D. A., et al. 2001, ApJ, 553, 121
Jørgensen, J. K., Schöier, F. L., & van Dishoeck, E. F. 2004, A&A, 416, 603
Jura, M. 1975, ApJ, 197, 575
Kaufman, M. J., Wolfire, M. G., Hollenbach, D. J., & Luhman, M. L. 1999, ApJ, 527, 795 (K99)
Le Bourlot, J. 2000, A&A, 360, 656
Le Bourlot, J., Pineau des Forêts, G., & Flower, D. R. 1999, MNRAS, 305, 802
Le Bourlot, J., Pineau Des Forets, G., Roueff, E., & Flower, D. R. 1993, A&A, 267, 233

Leitherer, C., et al. 1999, ApJS, 123, 3
Le Petit, F., Nehmé, C., Le Bourlot, J., & Roueff, E. 2006, ApJS, in press
Le Petit, F., Roueff, E., & Le Bourlot, J. 2002, A&A, 390, 369
Malhotra, S., et al. 2001, ApJ, 561, 766
Mandy, M. E., & Martin, P. G. 1993, ApJS, 86, 199
Martin, P. G., & Mandy, M. E. 1995, ApJ, 455, L89
McCartney, M. S. K., Brand, P. W. J. L., Burton, M. G., & Chrysostomou, A. 1999, MNRAS, 307, 315
Meyer, D. M., Cardelli, J. A., & Sofia, U. J. 1997, ApJ, 490, L103
Oey, M. S., & Kennicutt, R. C., Jr. 1993, ApJ, 411, 137
Parravano, A., Hollenbach, D. J., & McKee, C. F. 2003, ApJ, 584, 797
Péquignot, D., et al. 2001, in ASP Conf. Ser. 247, Spectroscopic Challenges of Photoionized Plasmas, ed. G. Ferland & D. Wolf Savin (San Francisco: ASP), 533
Regan, M. W., et al. 2004, ApJS, 154, 204
Savage, B. D., & Sembach, K. R. 1996, ARA&A, 34, 279
Shaver, P. A., McGee, R. X., Newton, L. M., Danks, A. C., & Pottasch, S. R. 1983, MNRAS, 204, 53
Shaw, G., Ferland, G. J., Abel, N. P., Stancil, P. C., & van Hoof, P. A. M. 2005, ApJ, 624, 794
Shibai, H., et al. 1991, ApJ, 374, 522
Smith, J. D. T., et al. 2004, ApJS, 154, 199
Sofia, U. J., Lauroesch, J. T., Meyer, D. M., & Cartledge, S. I. B. 2004, ApJ, 605, 272
Steiman-Cameron, T. Y., Haas, M. R., Tielens, A. G. G. M., & Burton, M. G. 1997, ApJ, 478, 261
Sternberg, A. 2004, in The Dense Interstellar Medium in Galaxies, ed. S. Pfalzner et al. (Berlin: Springer), 423
Sternberg, A., & Dalgarno, A. 1989, ApJ, 338, 197
Sternberg, A., Hoffmann, T. L., & Pauldrach, A. W. A. 2003, ApJ, 599, 1333
Tielens, A. G. G. M., & Hollenbach, D. J. 1985, ApJ, 291, 722
Wolfire, M., McKee, C. F., Hollenbach, D. J., & Tielens, A. G. G. M. 2003, ApJ, 587, 278
Wolfire, M., Tielens, A. G. G. M., & Hollenbach, D. 1990, ApJ, 358, 116
Wright, E. L., et al. 1991, ApJ, 381, 200